

*“Engineers like to solve problems. If there are no problems handily available, they will create their own problems”*  
Scott Adams

## **Chapter 6. Longitudinal Multi-Modal Assessment of Lung Cancer**

Abstract: In the following chapter, techniques previously discussed in this thesis are implemented in a systematic fashion to bring a comprehensive longitudinal multi-modal mouse lung cancer study to fruition. A Urethane induced mouse lung cancer model is used to investigate the biological changes of lung tumors over a 6-month period and evaluate an array of imaging modalities for early detection, diagnosis and characterization of lung cancer.

*In vivo* micro-CT imaging is implemented in the first stage of the study, which spans 6-months. Micro-MRI and micro-PET are utilized at the end of the 6-month time point to provide additional structural and functional information. Cellular imaging is performed using the LSCM and CBCM techniques on live and freshly excised lungs. All lungs are excised, fixed and rescanned using an *ex-vivo* micro-CT imaging approach. Lungs are then sectioned using the LIMA system and further processed for H&E histology.

Tumor growth rates within and across mice are calculated using the longitudinal micro-CT data. *In vivo* datasets from the micro-CT, micro-MRI and micro-PET are registered to histopathology providing a comprehensive array of information with the ability to correlate the non-invasive imaging modalities to the underlying histology. Finally, the utility of the CBCM technique for early diagnosis of lung cancer is investigated through analysis of normal, suspicious and tumor tissue acquired throughout the longitudinal mouse lung cancer study.

### **6.1 Introduction**

Small animal imaging is fast becoming a standard in preclinical biomedical research. The ability to track both disease and therapy provides for fast and efficient development of counteractive solutions. To date, no single imaging system has met

the requirements of all researchers. In recent times, multi-modal imaging has become a common term and practice in order to integrate the strengths of multiple imaging systems for solving biological problems.

Lung cancer, as described in Section 2.5, is a major health burden and is currently the leading cause of cancer death in the world [83, 84]. Many advances have been made in the past two decades for lung cancer detection and tracking, but the diagnosis and classification of lesions in their early stage is still generally not possible. The 5-year survival rate of 16% has remained consistent over the past thirty years. However, if we are able to diagnose and perform therapy at an earlier stage, the survival rate might reasonably be expected to significantly increase. Hence, development and investigation of new techniques for early diagnosis of lung cancer have become increasingly important.

In this chapter, we describe the development and integration of an array of imaging techniques developed and described over the span of this thesis for detection, tracking and characterization of lung tumors in the A/J Urethane mouse model of lung cancer. Through the accurate registration of multiple *in vivo* micro-CT datasets with their respective *ex vivo* micro-CT, LIMA and Histopathology datasets, a comprehensive picture of the progression and underlying cellular structure of lung tumors is attained.

Accurate correlation of histology back to *in vivo* datasets can provide a powerful means of understanding the relationship between tumor growth rates and underlying cellular manifestations. Currently, the spatial initiation and early progression of tumors in the A/J Urethane mouse model of lung cancer is unknown and cannot be accurately determined using standard histology techniques. Also, the correlation of tumor growth rate to the underlying histology has not been thoroughly investigated, and is only possible using non-invasive assessment of tumor growth.

In a recent study, micro-MRI was utilized for tracking the growth of tumors in the Urethane mouse model of lung cancer. In this study, tracking was initiated at 8 months post Urethane administration, and tumors smaller than 0.5mm were not detectable; however, it is unlikely tumors less than 1mm would be reliably detected

using such a technique [202]. In an earlier study, micro-CT imaging was used for lung tumor tracking, but no respiratory gating was performed, and very limited quantitative results were presented [160]. These previous studies have only been presented to justify the use of non-invasive imaging modalities for identification, tracking and analysis of tumors in mice with no thorough investigation of the growth rates with respect to the underlying biology [39, 157, 159].

Finally, the capacity to visualize the underlying histology of suspicious regions *in vivo* using a fiber optic catheter based imaging system, a critical step towards early characterization and diagnosis of lung cancer in the clinical situation, has never been undertaken in this mouse model of lung cancer.

## **6.2 Material and Methods**

### **6.2.1 Micro-CT Imaging Heating Chamber**

Maintenance of mouse vital signs during imaging is of paramount importance within a longitudinal study. Maintaining a constant body temperature is extremely important for small animals, such as mice, that have a large body surface to volume ratio. This risk of hypothermia is further compounded when mice are under anesthesia. The Siemens Micro-CAT II scanner has multiple large cooling fans inside the enclosure, maintaining cool temperatures for the X-ray source and CCD detector. When this system is configured for high-resolution imaging, the mice have no protection from the circulating air. Mice are subjected to a continuous cool breeze that dramatically reduces their body temperature and increases their risk of hypothermia and mortality.

A custom imaging chamber has been designed and built to block the circulating air and provide a protected space for the mouse. A 75-watt infrared heat lamp has been mounted inside the micro-CT scanner. When the imaging chamber is installed, the heat lamp becomes sealed within the chamber. An electronic temperature controller connected to the heat lamp has also been installed in order to maintain a user-defined temperature within the chamber. The chamber is shown in Figure 6.1.

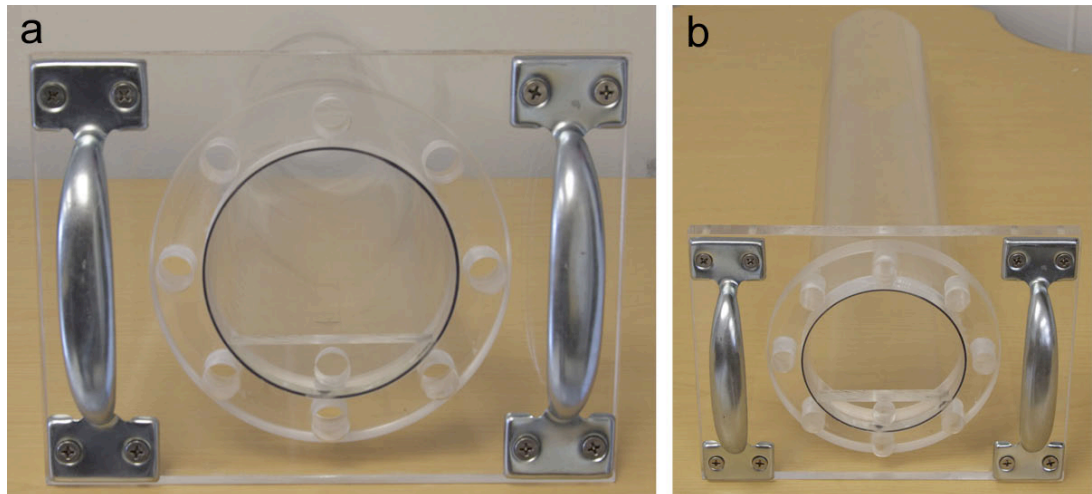


Figure 6.1: Custom tunnel heating chamber.

### 6.2.2 Flexible Miniature Mouse Bronchoscope

As described in earlier chapters, imaging the lung *in vivo* has many obstacles and is considered extremely problematic. Particularly challenging is the correction or prevention of motion artifacts due to breathing. The micro-CT breath hold technique developed and described in Section 4.3 requires mechanical ventilation of the mouse in order to control the respiratory phases. For longitudinal studies, a tracheotomy as performed in Section 4.3 is unacceptable, and non-invasive intubation is mandatory. Intubation of small animals, such as mice, is extremely difficult to perform safely and repetitively without injuring the animal. From the previously described techniques and tools [203-207], one can conclude that visual identification of the vocal chords and validation that the intubation tube is located inside the trachea are the two most difficult aspects. Visual guidance using a bronchoscope would be extremely advantageous and reduce the number of misses and decrease the mortality rate.

A miniature mouse bronchoscope has been designed and built in order to overcome the discussed obstacles. The bronchoscope is composed of three main components, an optical viewfinder, a coherent fiber optic imaging bundle and a Gradient-Index (GRIN) lens. The proximal end of a mouse trachea has a diameter between 1-1.5mm with the vocal chords smaller still, therefore a bronchoscope with a diameter less than 1mm was required to enter the trachea. In order to use a 22-gauge catheter for

intubation and have the bronchoscope feed through the catheter as to facilitate fast and efficient intubation, an outer diameter of less than 0.6mm was needed. Figure 6.2 represents the constructed endoscope with an outer diameter of 0.5mm at the distal tip.

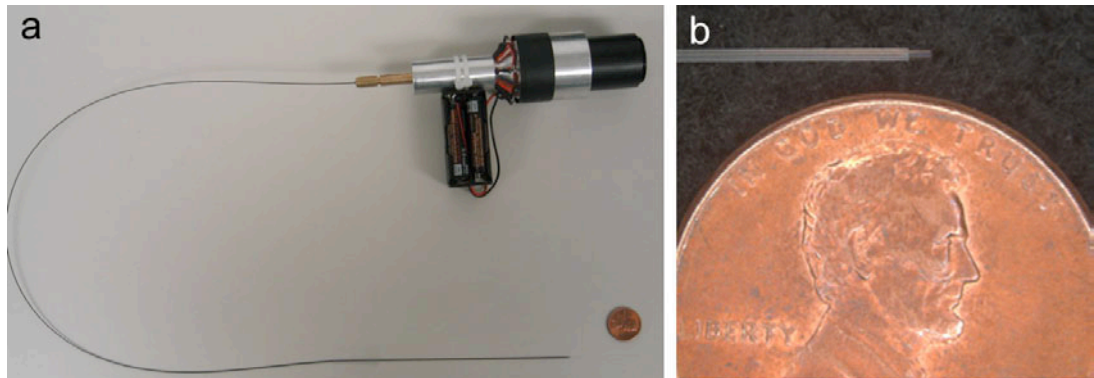


Figure 6.2: (a) mouse endoscope with optical viewfinder, (b) magnified image of bronchoscope tip against a United States penny.

Using this bronchoscope, we can perform mouse intubation safely and efficiently, and with direct visual guidance mice are intubated on the first attempt. Figure 6.3 (a) illustrates a digital image acquired through the optical viewfinder during a mouse bronchoscopy procedure, and Figure 6.3 (b) illustrates the vocal chords.

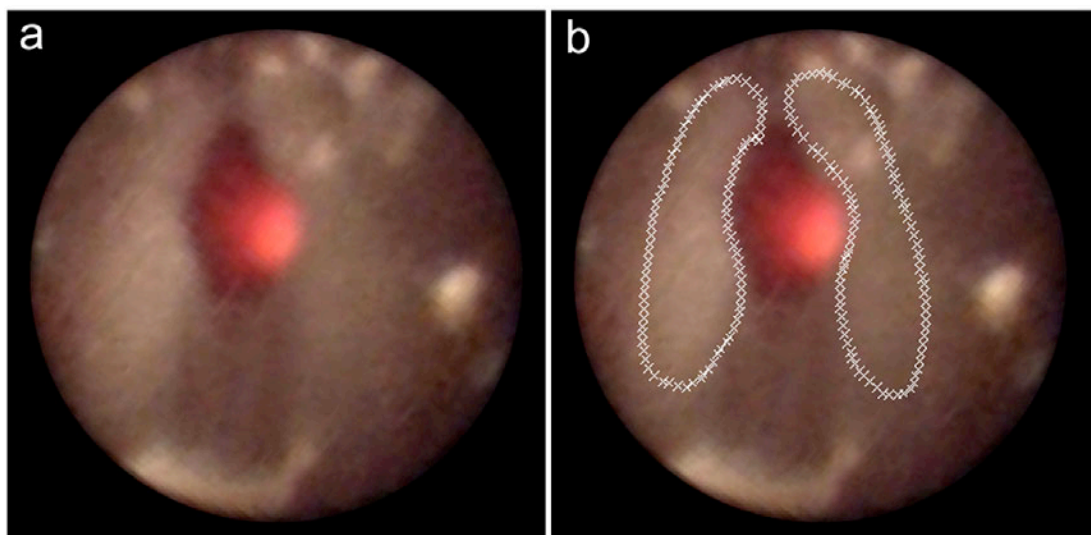


Figure 6.3: Mouse-bronchoscopy - image acquired at the vocal chords, (a) original image, (b) image with dashed outline of vocal chords. Bright red light in the trachea is a result of the snake light placed over the chest wall, and aides in guidance.

### 6.2.3 Portable Micro-Controller Ventilator

The breath hold technique described in Section 4.3 utilizes a computer controlled Flexivent ventilator (Scireq, Montreal, Quebec) and LabVIEW (National Instruments, Austin, Texas) software for accurate gating. This experimental setup requires two desktop computers that take considerable space and are not mobile. In the *in vivo* imaging techniques described in Section 5.3 and utilized in this chapter, a portable system with a small footprint is required for transport into the microscopy facility. The Intermittent Iso-pressure Breath Hold (IIBH) technique was translated into a hardware based triggering system for use with a Columbus CIV-101 (Columbus Instruments, Columbus, Ohio) portable small animal ventilator. The layout for the micro-controller circuit is shown in APPENDIX A Figure A1. The complete ventilator and triggering system is shown in Figure 6.4.

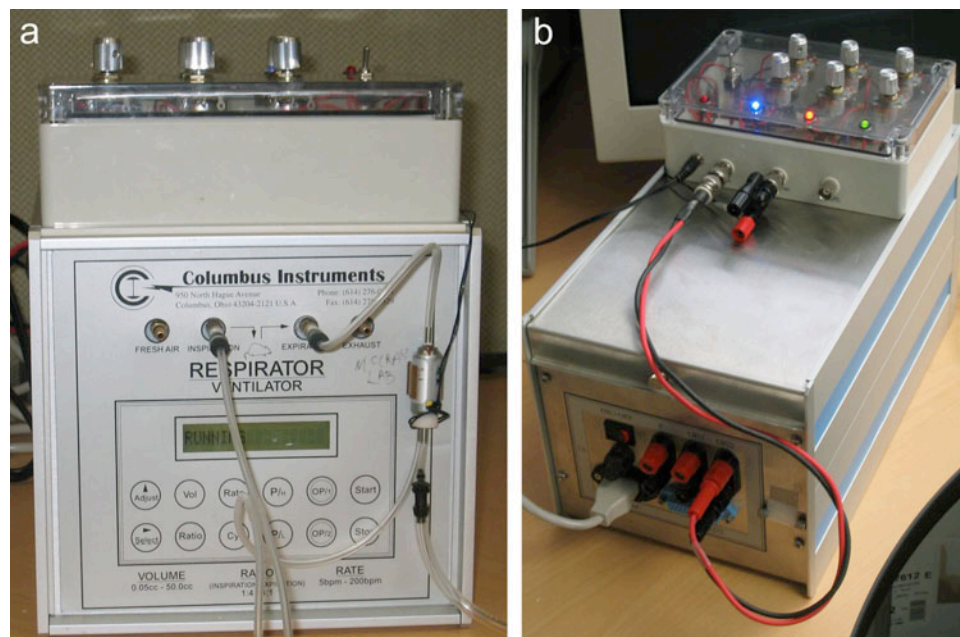


Figure 6.4: Small animal ventilator with custom respiratory gating micro-controller.

In addition to the micro-controller ventilator, an electronic pressure controller was also built specifically for low-pressure control associated with breathing i.e. 0- 50 cmH<sub>2</sub>O; this system is shown in Figure 6.5. Inside the enclosure is a piezo electric double pneumatic solenoid (Bellofram Precision Control, Newell, West Virginia), controlled using a proportional integrative derivative (PID) microcomputer, which can be set to any pressure between 0-50 cmH<sub>2</sub>O. This system allows highly accurate

and constant (iso) pressures with a tight tolerance to be fed and maintained through the entire breath-hold imaging period.



Figure 6.5: Custom electronic pressure controller.

## 6.2.4 Animal Preparation

Experimental procedures carried out in this study were approved by the University of Iowa Animal Care Committee. Mice underwent intervention in four distinct scenarios: mice were anesthetized for administration of the Urethane administration, mice were placed under anesthesia for each micro-CT scan, select mice were anesthetized in the final round of micro-CT imaging for subsequent MRI and PET scan, and mice were placed under anesthesia for the *in vivo* laser scanning confocal microscopy experiment. This study began with 16 normal A/J mice aged between 6-8 weeks, weighing between 13-20 grams. Each imaging protocol required a specific animal protocol as outlined below:

### 6.2.4.1 Urethane administration protocol

Twelve of the sixteen mice were administered with Urethane (Sigma-Aldrich, St Louis). Each mouse was initially sedated using 3-5% isoflurane, the mice were then weighed and injected I.P. with 1mg/g Urethane dissolved in 0.9% NaCl Saline. Mice were tagged with ear tags (Harvard Apparatus, Massachusetts, USA) and placed back into their respective cages and allowed to recover. As Urethane is a

known anesthetic agent, mice administered with Urethane generally required 30 minutes longer to regain consciousness.

#### **6.2.4.2 Micro-CT animal protocol**

Prior to imaging, mice are sedated using 3-5% isoflurane, weighed and injected intra muscular (IM) in the right hind leg with 1.0mg/mg medetomidine hydrochloride and 40.0-80.0mg/kg ketamine. This anesthetic regiment was determined empirically in order to reduce total anesthesia while maintaining sufficient sedation for restraining mice during the intubation phase. Mice were transferred to an intubation table where a miniature fiber optic bronchoscope (as outlined in section 6.2.2) was utilized to intubate the mice with a 22-gauge 1 inch Teflon catheter (Becton Dickinson, Utah, USA). Triple anti-biotic ointment was placed over the eyes, in order to maintain moisture during the imaging phase, as the anesthesia inhibits spontaneous blinking. Mice were placed supine onto a polystyrene bed, and mounted onto the Micro-CT carbon fiber animal stage. Using perforated tape (3M, Minnesota, USA) mice were secured at the limbs and ECG and temperature sensors were attached for physiologic monitoring using a BioVet C1 data acquisition system (Supertron Technologies, Newark, New Jersey). Respiratory paralysis was achieved by administering 0.5mg/kg of rocuronium IM in the left hind leg. The tracheal catheter was then connected to the computer controlled Flexivent ventilator (Scireq, Montreal, Quebec) and the mice were ventilated at 120br/min and tidal volume of 15ml/kg. Isoflurane was set to 1-2% for maintenance of sedation throughout the imaging protocol. A heat lamp and heating chamber was created, as outlined in section 6.2.1, and used to maintain body temperature during scanning to reduce hypothermia, which is a major contributor to mortality during anesthesia. Finally, 0.5mls of PBS was injected subcutaneously (SC) above the abdomen in order to prevent dehydration during the imaging period.

#### **6.2.4.3 Micro-PET animal protocol**

Two compounds were given to mice for PET imaging, Fludeoxyglucose F18 (18F-FDG) and Fluorothymidine F18 (18F-FLT). 18F-FDG a glucose analog is taken up by glucose metabolizing cells where malignant tumors have an elevated uptake of

glucose and can be identified using the  $^{18}\text{F}$ -FDG PET marker.  $^{18}\text{F}$ -FLT is a relatively new PET marker proposed for identification of tumor proliferation.

To reduce metabolic intake, food and bedding was removed from the mouse cage, with water still available six hours prior to PET scanning. Mice were weighed and anesthesia induced initially at 3-5% isofluorane and maintained at 1-1.5%. To determine the dosage of  $^{18}\text{F}$ -FDG given to each mouse, a blood glucose measurement was obtained using a Theresense (Abbott, Illinois, USA) monitor. In addition, to calibrate the uptake of the  $^{18}\text{F}$ -FDG from the PET imaging the following steps were undertaken. Measurement of the stock  $^{18}\text{F}$ -FDG microfuge tube was made in the dose calibrator. 0.0750 cc of  $^{18}\text{F}$ -FDG was drawn up into a 0.3cc Insulin syringe and the residual  $^{18}\text{F}$ -FDG in the microfuge tube was measured in the dose calibrator. 0.050cc  $^{18}\text{F}$ -FDG was injected into the right eye's intra-orbital space. Mice were injected with 0.2cc saline subcutaneous in the scapular region for hydration during imaging. Mice were then placed back into a cage while under isofluorane anesthesia for 30 minutes to allow uptake of  $^{18}\text{F}$ -FDG. Mice were then placed onto the Plexiglas scanning bed in the prone position. Three 5min PET scans were performed under 1-1.5% isofluorane anesthesia. Once scanning was complete, the isofluorane was shut off and the mouse was placed back into the cage for recovery.

A tail vein injection variation of this protocol was also used. Here, 0.150cc  $^{18}\text{F}$ -FDG and 0.050cc saline was injected in the tail vein rather than the retro-orbital injection as outlined above. Prior to injection, mice were placed under a heat lamp for five minutes to encourage vasodilatation of the tail vein, assisting the injection process.

Finally, an  $^{18}\text{F}$ -FLT protocol was also implemented for measuring the cell proliferation index. In this case, a tail vein injection was performed with 0.150cc  $^{18}\text{F}$ -FLT and 0.050cc saline, and 60min was allowed for uptake. Also 30min prior to injection of the FLT agent, 2mg/kg of 5-Fluoro-2'-deoxy-uridine (FuDR) was administered in order to reduce the baseline cell proliferation of the mouse, thereby allowing greater uptake of the FLT by potentially aggressive tumor cells.

#### 6.2.4.4 Micro-MRI animal protocol

Mice were initially sedated using 3-5% isoflurane followed by an IP injection of 87.5mg/kg ketamine and 12.5mg/kg xylazine. Mice were positioned prone inside a quadrature RF coil with 25 mm inner diameter and usable imaging length of 30 mm (Doty Scientific, Columbia, SC). Scout images were first acquired to verify correct positioning of the lungs inside the coil.

At the completion of the scan, mice were placed back into their cage for recovery.

#### 6.2.4.5 LSCM *in vivo* animal protocol

Mice were initially sedated using 3-5% isoflurane followed by an IP injection of 87.5mg/kg ketamine and 12.5mg/kg xylazine. Following a negative pedal reflex test, 50mg/kg sodium fluorescein was administered IP and allowed ten minutes for uptake. A tracheotomy was performed via a mid-line incision and insertion of a 20-gauge catheter as shown in Section 5.3, Figure 4.24. Mice were then mechanically ventilated using a modified Columbus CIV-101 (as outlined in Section 6.2.3). A thoracotomy was performed, and the chest wall was surgically removed revealing the lung and heart. This was performed carefully ensuring no lacerations were made into the lung parenchyma in order to avoid punctures.

Between image acquisitions, mice were ventilated at 120br/min and 0.5ml tidal volume with room air. During imaging, a 5 second breath-hold was induced at a user defined pressure level using a custom developed microcomputer pressure controller system (as outlined in Section 6.2.3) [199].

Mice vital signs were monitored using an ECG and pulse oximetry meter (Tyco Healthcare, California, USA). The ECG probes were attached to the paws, while the pulse oximeter sensor was modified and attached to the tail.

Figure 6.6 represents the mouse prior to the tracheotomy and thoracotomy. Figure 6.7 represents the *in vivo* catheter based confocal microscopy (CBCM) imaging setup including the desktop LSCM, fiber optic probe, ventilator, ECG and Pulse Ox meter.

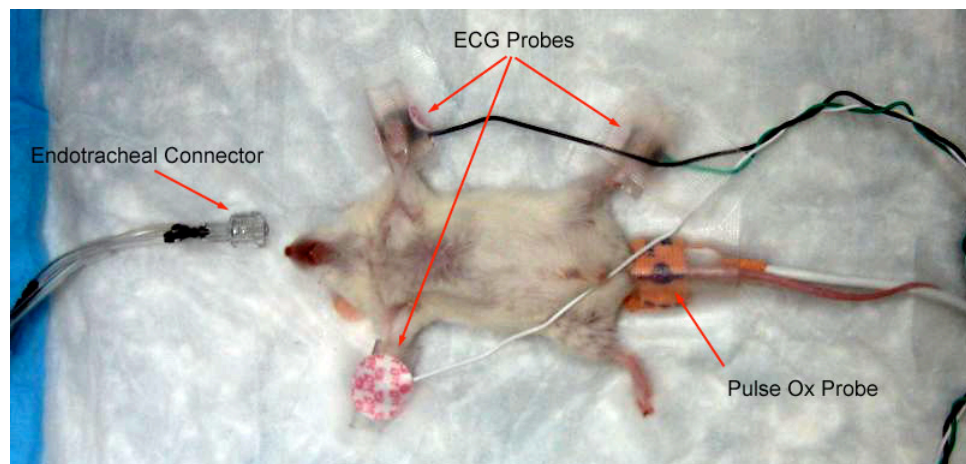


Figure 6.6: Mouse connected to ECG and Pulse Ox sensors prior to Tracheotomy.

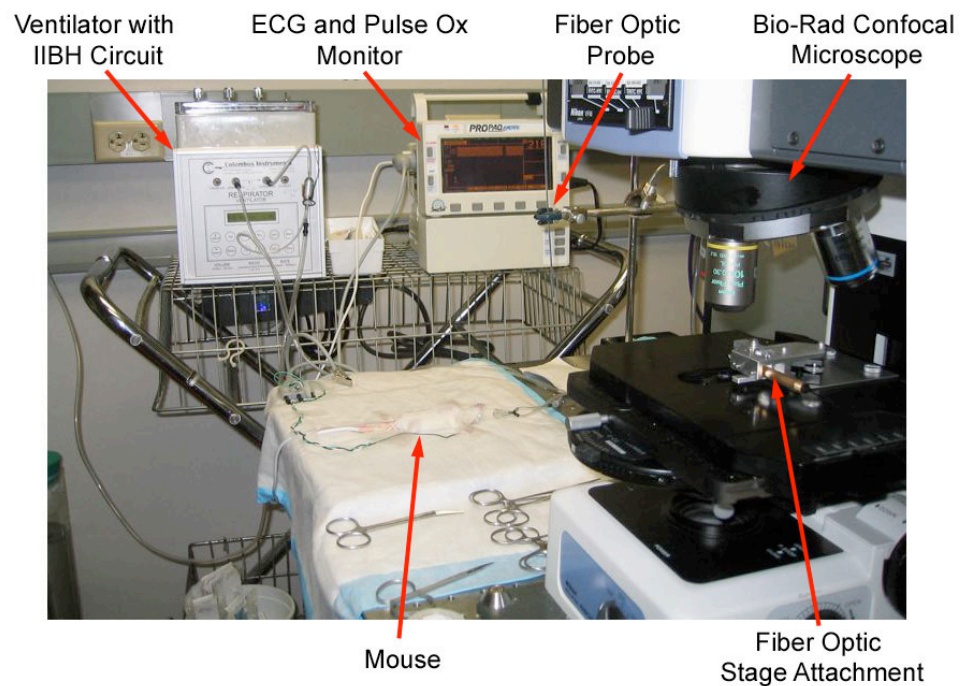


Figure 6.7: *in vivo* CBCM mouse lung imaging setup.

### 6.2.5 Study Timeline

Mice were imaged in four groups of three mice: the first group was imaged using the *in vivo* micro-CT technique at 2 and 3 months post Urethane administration, the second at 2, 3 and 4 months, the third at 2, 3, 4, and 6 months, and finally the fourth group at 6 and 9 months. At each end point, mice were imaged using the CBCM and LSCM techniques followed by the *ex vivo* imaging protocols, as outlined above. The

fourth group of mice was also imaged using the micro-MRI at 6 months and the micro-PET system at 6 and 9 months. A timeline of the study is shown below in Figure 6.8.

Imaging Modalities <i>Yellow: Group 1, Blue: Group 2, Green: Group 3/ Normals , Red</i>	Months Post Urethane Administration										
	0	1	2	3	4	5	6	7	8	9	
<b>Delivery of Mice and Administration of Urethane</b>	G1	G2	G3/N	G4							
<b><i>In vivo</i> micro-CT imaging</b>			G1 G2 G3/N	G1 G2 G3/N	G2 G3/N		G3/N G4			G4	
<b><i>In vivo</i> micro-MRI imaging</b>							G4				
<b><i>In vivo</i> micro-PET imaging</b>							G4			G4	
<b><i>In vivo</i> CBCM and <i>ex vivo</i> LSCM imaging</b>			G1		G2		G3/N			G4	
<b><i>Ex vivo</i> micro-CT, LIMA and Histology</b>			G1		G2		G3/N			G4	

Figure 6.8: Gantt chart representing the timeline for the four groups of Urethane mice and single normal group in this study.

## 6.2.6 Multi-Modal Image Acquisition

### 6.2.6.1 Micro-CT image acquisition

The *in vivo* micro-CT breath-hold imaging technique, as outlined in Section 4.3, was used for the longitudinal micro-CT scans in this study. In brief, the micro-CT X-ray source was set to 60 kVp and 500  $\mu$ A tube current. The CCD detector was set to 500 ms exposure, binning of 2 and the system was configured to acquire 720 projections over 200 degrees (half-scan) with 100 bright and dark calibration images. Each projection produced a 1536x1024 pixel image with a pixel spacing of 28 microns. Respiratory gating was performed using a combination of a computer controlled Flexivent (Scireq, Montreal, Quebec) ventilator, LabVIEW program and electronic solenoid triggering system, as outlined in Section 4.3.

### 6.2.6.2 Micro-PET image acquisition

Micro-PET imaging was performed on a Phillips MOSAIC animal PET scanner (Phillips Medical Systems, Milpitas, CA). Each mouse was positioned within the sensitive region of the scanner. Three images were acquired at five minutes each from the same bed position. A total of 240 256x256 pixel transverse slices of 0.5mm thickness were reconstructed.

No respiratory gating was performed during image acquisition.

### 6.2.6.3 Micro-MRI image acquisition

Magnetic resonance imaging (MRI) was performed on a Varian Unity/INOVA 4.7 Tesla (200 MHz) small bore MRI scanner (Varian Inc., Palo Alto, CA). This magnet is equipped with 270 mT/m gradients capable of 0.1 ms rise time.

A high-resolution volume acquisition was performed with a 3D gradient-recalled echo (GRE) pulse sequence. The axial volume imaged covered 27mm x 27mm x 18mm with an imaging matrix of 256 x 128 x 32 for a resulting resolution of 0.1mm x 0.2mm x 0.6mm. Relevant imaging parameters included TR/TE = 20/4 ms and 3 signal averages to improve image quality for a total scan time of approximately 5 minutes.

No respiratory gating was performed.

### 6.2.6.4 LSCM *in vivo* image acquisition

The catheter based confocal microscopy (CBCM) technique, outlined in Section 5.3, was used for the *in vivo* confocal lung imaging. In addition, to the techniques outlined in Section 5.3, several additional methods were developed for assessing tumor pathology.

In order to identify alveolar macrophages using the LSCM and CBCM technique, PKH26-PCL, a fluorophore, was administered into the tail vein 24 hours prior to imaging. PKH26-PCL selectively labels phagocytic cells such as monocytes, macrophages and neutrophils by forming a dye aggregate, which significantly

inhibits uptake of the dye by non-phagocytic cells. PKH26-PCL is a two-part solution one is the diluent and the second is the PKH26-PCL dye (1000 $\mu$ M/ml), once diluted to a concentration of 100 $\mu$ M/ml; 0.2cc is injected intravenously (IV) into the tail vein. Once injected into the bloodstream, the dye is taken up by monocytes through a phagocytic process. Labeled monocytes recruited into the alveolar space as macrophages are then labeled with the PKH26-PCL dye.

Acridine Orange is topically applied to the region of interest at a concentration of 0.5mg/ml. Acridine Orange is a cell permeant nuclear stain that can be used for *in vivo* experiments. This dye has a unique property where it emits green fluorescence when bound to double stranded DNA (dsDNA) and emits red fluorescence when bound to single stranded DNA (ssDNA). This makes Acridine Orange a very useful nuclear stain for cell-cycle assessment. The presence of ssDNA indicates active mitoses, an important marker for cancer cells.

Draq5 is another cell permeant nuclear stain for use in live cell imaging with an emission spectra in the far red. This property allows this stain to be used in combination with many other common dyes that emit in the blue-orange region of the spectrum. 1-2 $\mu$ l of Draq5 is topically applied to the region of interest at a concentration of 5mM.

In addition, when imaging using multiple stains, each frame was acquired using three Photo Multiplier Tubes (PMT) at three distinct spectral ranges. The first included 500-530nm, the second from 560-620nm and the final was 660nm+. Three images per frame were composed into a single RGB pseudo color image, where red represented the first spectral range, green the second and blue the third, i.e. emission from the red region (660+) was represented by the pseudo color blue. Depending on the stains that were applied to the tissue of interest, three lasers were powered individually or simultaneously during image acquisition. These include a 488nm, 543nm, and 637nm laser.

### **6.2.6.5 *Ex vivo* micro-CT & LIMA image acquisition**

The LIMA system as outlined in Chapter 3 was used in this study to register the *in vivo* micro-CT, MRI and PET images to histology.

Once each mouse had undergone the LSCM imaging, the lungs were excised and fixed using the techniques outlined in Section 3.2.7; in brief, the lungs were fixed via intra-tracheal instillation with a modified Heitzman technique maintaining the radio-density of the tissue, thereby allowing radiological comparison. After 12-24 hours of liquid fixation, lungs were connected to a user defined air pressure system and placed inside a heated oven set to 60 degrees Celsius for 2 days. Fixed lungs then underwent a foam embedding procedure (outlined below) to maintain the orientation of the lung between subsequent *ex vivo* micro-CT imaging scans and LIMA sectioning and imaging. This maintenance of orientation between these two modalities is critical in allowing accurate registration of the initial *in vivo* scans to the final histology slides.

#### ***Polyurethane whole lung foam embedding***

A foam embedding procedure was implemented for this study in order to maintain the orientation between the *ex vivo* micro-CT scan and the LIMA sectioning and imaging. A custom mold was designed and built, as shown in Figure 6.9. The embedding procedure consists of a two-step foam encasing. Firstly, the lung is coated with a polyurethane foam (2lb kit, US Composites, Florida) mixture in free space to ensure its final orientation inside the mold and to inhibit the foam from compressing the lung during the second foam expansion process.

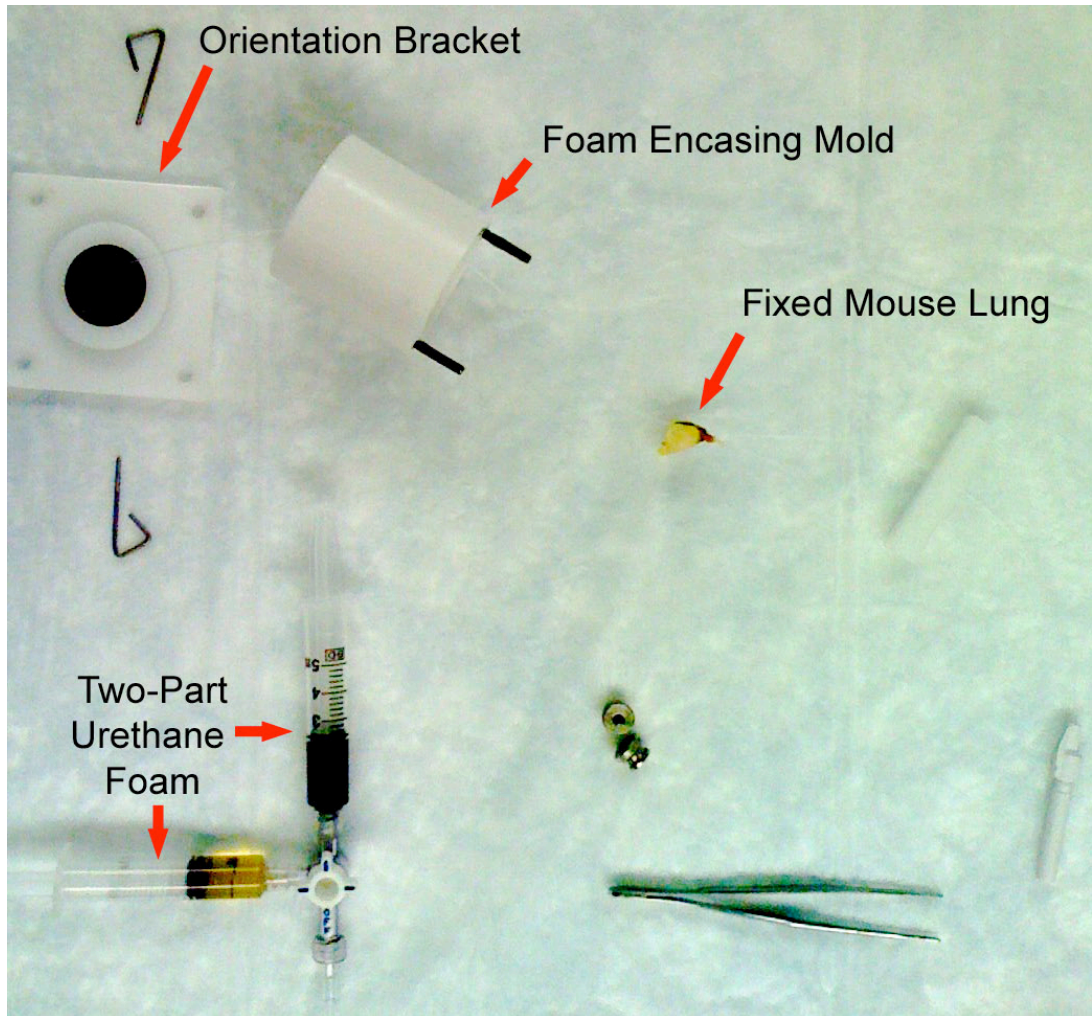


Figure 6.9: Custom lung embedding equipment including the orientation bracket, foam encasing mold and two-part polyurethane foam.

The lungs were initially connected to a fishing line suspended in air connected to a stand and the base of the orientation bracket as shown in Figure 6.10. A suture was tied between the trachea and the fishing line to maintain the correct orientation during foam embedding. A second suture was looped around the center of the lung and the fishing line in order to hold the lobes together during embedding.

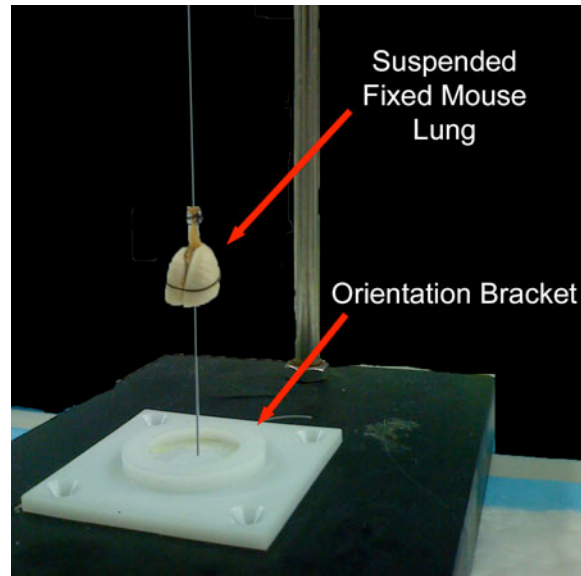


Figure 6.10: Mouse lung suspended with fishing line and tied in place with one suture around the trachea. A second loose suture loop is placed around the lung and fishing line in order to maintain lobe positions during embedding.

The lung was positioned as described in order to reflect its natural orientation (although vertical) in the mouse with the fishing line representing a plane parallel to the micro-CT animal stage. A two-part polyurethane foam (2lb kit, US Composites, Florida) was then created using a modified mixture containing 2ml part A (isocyanate), 2.1ml part B (polyurethane resin) and 0.01ml Indian ink. The Indian ink was added in order to increase the contrast between the normally yellow foam and lung tissue during subsequent LIMA imaging. Each component was initially placed in a 5ml syringe connected to a three-way lure lock connector. The two syringes were then mixed into one another vigorously for 25 seconds. This setup allowed for fast mixing of the two components ensuring a consistent foam product. The lung was then completely covered in a thin layer of the foam mixture. Once this first foam process had set (usually within 30 minutes), the lung was completely covered with foam.

The foam encased lung was then translated down to the base of the orientation container. The cylindrical mold was placed over the lung and mounted to the base. A beam was placed over the cylinder and the fishing line was passed through the central hole. The foam-covered lung was now suspended inside the mold with access from both the sides of the beam.

A second foam mixture, as outlined above, was prepared and poured into the mold ensuring the lung was stationary during foam expansion. The foam was allowed to set for 30 minutes and the beam, cylinder and fishing line were removed, leaving a tapered cylindrical block of foam mounted to the base of the orientation bracket as shown in Figure 6.11.



Figure 6.11: Foam encased mouse lung mounted to the base of the orientation bracket.

The orientation bracket and foam block can then be mounted onto a custom micro-CT axial imaging attachment and a subsequent LIMA tissue stage attachment, ensuring that the axial micro-CT images are parallel to the imaging plane of the LIMA microscope. Figure 6.12 represents a schematic illustration of this process.

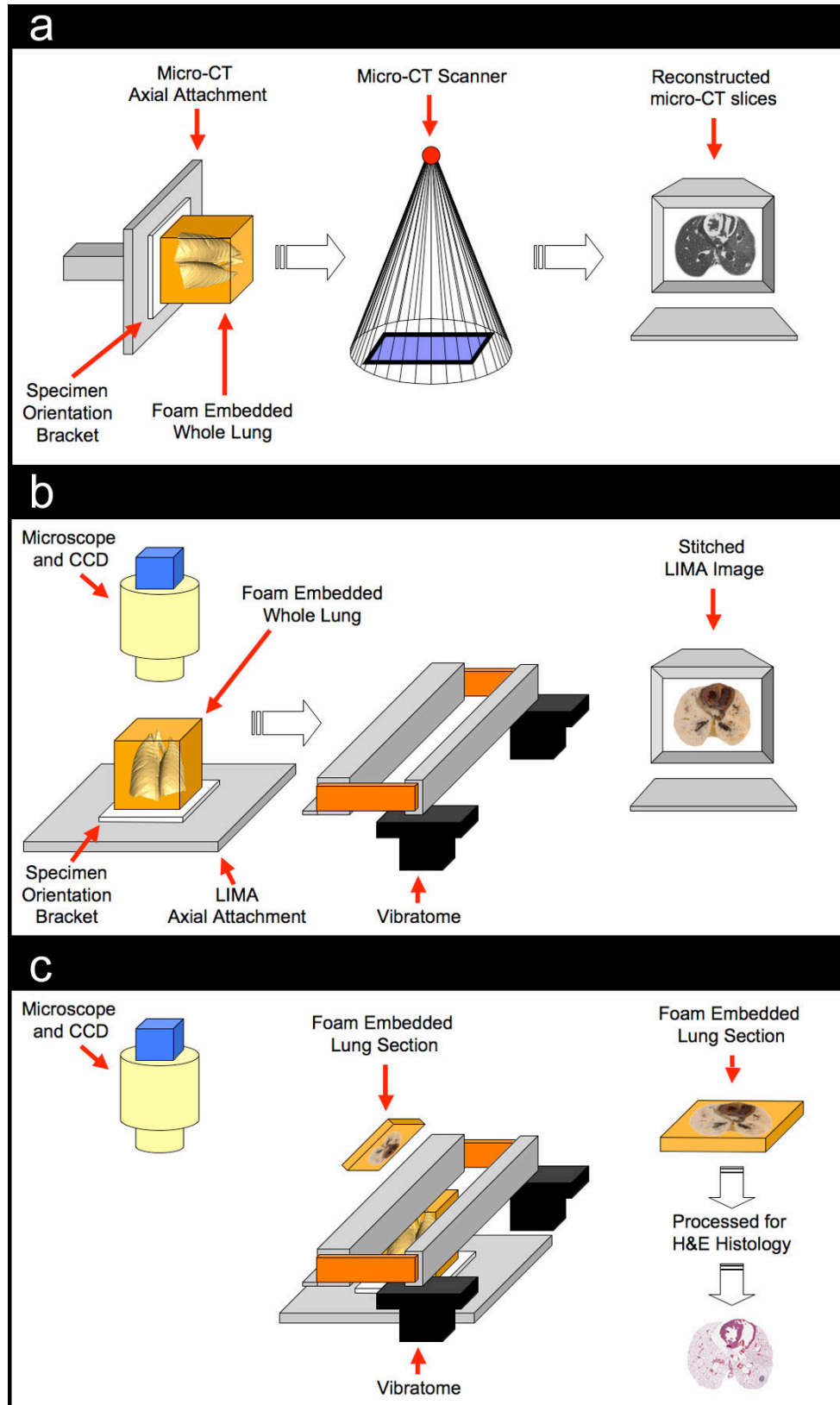


Figure 6.12: Schematic illustration of the *ex vivo* image acquisition process utilizing the orientation bracket, during (a) micro-CT imaging, (b) LIMA imaging and (c) LIMA sectioning and H&E Histology processing.

### ***Ex vivo micro-CT imaging***

Lungs embedded in foam were scanned on the micro-CT under four separate protocols: one standard soft tissue imaging protocol used for registration of *in vivo* datasets to the LIMA and histology datasets, one for high-resolution analysis and finally two for future dual-energy subtraction analysis. All scanning was performed using the Siemens Pre-Clinical MicroCAT II Scanner, as detailed in Chapter 4.

#### **Standard Soft Tissue Protocol**

A soft tissue scan was setup using 60kVp and 368uA X-ray energy providing a 30 micron spot size. 721 projections were acquired over 200 degrees at 1536x1024 28 micron equivalent pixels. The exposure time was set to 2250ms. This scan provides the closest equivalent to the *in vivo* micro-CT scans and becomes the basis for registration across the imaging modalities.

#### **High-Resolution Protocol**

The high-resolution scan was setup using 80kVp and 150ua X-ray energy providing a 15 micron spot size. 721 projections were acquired over 200 degrees at 1792x1280 14 micron equivalent pixels. The exposure time was set to the maximum 8960ms in order to use the maximum dynamic range of the 12bit CCD camera, ensuring greater Signal to Noise Ratio (SNR). Note that this scanner can be configured for higher-resolution scanning, but the enclosure must be removed, the camera and detector manually must be moved and finally a re-calibration of the geometry must be performed. The scanning time for the four scans detailed here already required approximately four hours, and it was deemed unfeasible to add another three hours to gain an extra five microns of resolution.

#### **Dual-Energy Protocol**

A low-energy scan of 40 kVp was performed with no hardware filter. A second high-energy scan of 120 kVp was performed with a 3 mm Aluminum hardware filter. The current was set to 500 uA and 184 uA, respectively, to maintain the focal spot size of the X-ray source between the two scans. Also, the exposure time was set to 2500 ms and 1750 ms, respectively, to maintain an equivalent dosage/noise level

between the scans. Both scans were acquired over 360 degrees with a total of 721 projections at 1536x1024 28 micron equivalent pixels. The dual energy scans were acquired over the 360 degree rotation to reduce beam hardening heterogeneity in the field of view, thereby allowing greater accuracy in subsequent subtraction.

### ***LIMA imaging***

The LIMA system was setup to perform white light imaging at 30x magnification. 30 image tiles (5x6) at 1300x1050 each and 2 micron equivalent pixels were acquired en-bloc. Image tiles were acquired with 15% overlap in both the horizontal and vertical direction. The microtome was setup to section 500 microns per image acquisition. As outlined in Chapter 3, sections are commonly in the range of 250 microns, but in this study thicker sections were chosen since the reproducibility of the histology was more important than isotropic LIMA acquisition. For each lung there were between 30-40 sections acquired from the apex to base of the lung.

#### **6.2.6.6 Histology image acquisition**

Sections removed from the LIMA system were wrapped in biopsy paper (Surgipath Medical Industries Inc., Richmond, Illinois), placed in histology paraffin embedding Histosette I cassettes (Simport, Beloeil, Quebec) and sent to pathology. Twenty 5 micron H&E histology slides were prepared for each 500 micron LIMA tissue section. Ten of these slides represented tissue sections every 25 microns, and ten were acquired serially back-to-back at the center of the tissue block.

Microscope slides were digitized using a Scan Scope automated slide digitizer (Aperio, California, USA) incorporating a dynamic focusing system in order to maintain focus through out the slide acquisition process in spite of uneven tissue preparation. Slides were scanned using a 20x objective resulting in an equivalent pixel size of 0.504 $\mu$ m.

## **6.2.7 Image Processing**

### **6.2.7.1 Micro-CT image processing**

Micro-CT images acquired under the protocol outlined in Section 4.3 underwent several processing steps prior to reconstruction, as outlined in Section 4.2. In brief, each dataset was calibrated for the flat field and bright images followed by a filtering step to reduce line artifacts in the sinograms, which would otherwise result in ring artifacts in the reconstructed images. Finally, the Feldkamp reconstruction was executed using a dynamic center offset and source to object distance look up table developed in Section 4.2.

Since the micro-CT system is not a turnkey system and needs to be customized to each application for optimal results, these processing steps are important for accurate analysis.

The output of the reconstruction was then converted into both a DICOM and raw 16bit signed images for subsequent analysis.

### **6.2.7.2 Micro-PET image processing**

PET images were converted into the DICOM format and used for subjective visualization and assessment of FDG and FLT uptake; no further processing was performed.

### **6.2.7.3 Micro-MRI image processing**

MRI images were converted into the DICOM format and used for direct visualization of the thoracic region; no further processing was performed.

### **6.2.7.4 LSCM image processing**

Images acquired using the *in vivo* LSCM protocol were processed as outlined in Section 5.3.2.3. In brief, each frame in the CBCM dataset was subtracted from a

background image and low pass filtered to remove the fiber matrix pattern. Images were then saved as 16bit Tiff's and used for visualization and analysis.

#### **6.2.7.5 LIMA image processing**

Each section from the LIMA image contains 30 sub-tiles that were stitched and montaged into one large composite. This process was performed using the semi-automated Photomerge algorithm in Adobe Photoshop (Adobe Systems Inc., San Jose, California).

#### **6.2.7.6 Histology image processing**

Histology slides digitized using the Scan Scope automated slide digitizer (Aperio, California, USA) were compressed into a tiled JPEG format and exported as a single pyramidal tiff image. An image of each tumor was then extracted at 2, 4, 10, and 20x magnification using the Aperio Viewer application.

### **6.2.8 Image Analysis**

#### **6.2.8.1 Micro-CT tumor growth analysis**

*In vivo* micro-CT images acquired at each time point for each mouse were converted into the DICOM format. Each data set was imported into a commercial prototype oncology program (OncoCare, Siemens, NJ), as shown in Figure 6.13.

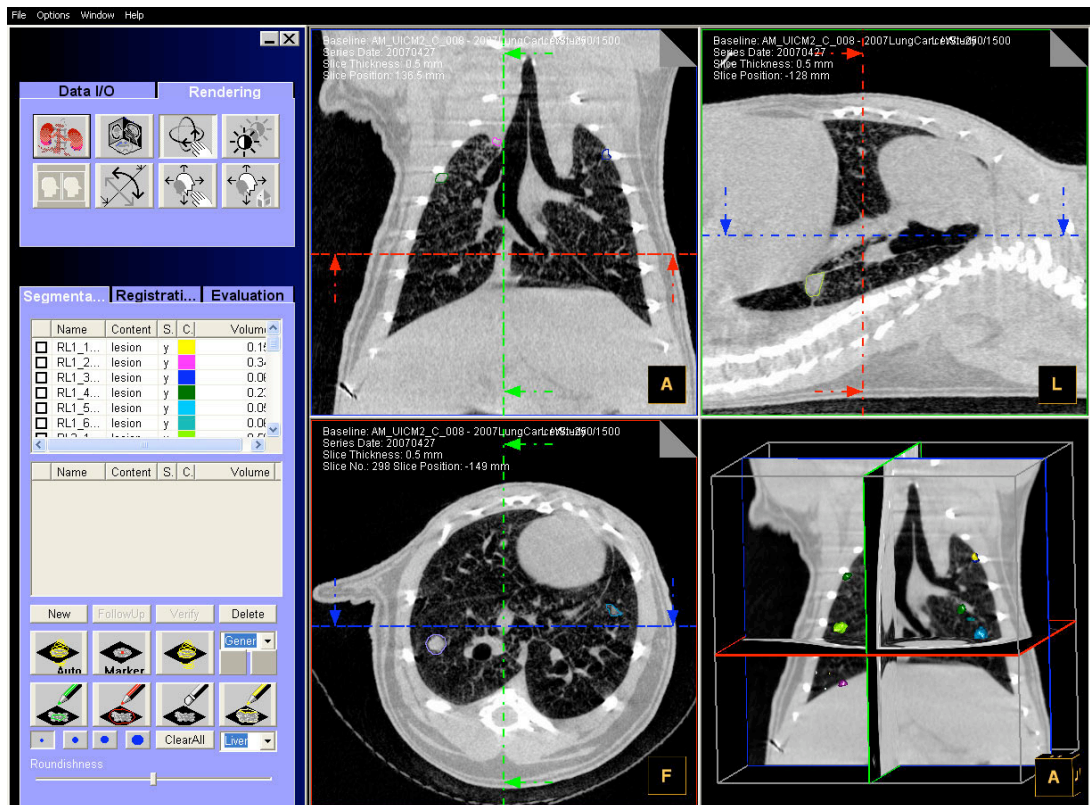


Figure 6.13: Siemens OncoCare prototype application used to facilitate in semi-automated segmentation of mouse lung tumors.

Tumors were located manually by the user and traced using a semi-automated segmentation routine [208]. First a straight line or stroke across the cross-section of the tumor was drawn, keeping each end of the line close to the boundary of the tumor. The program then automatically performs three main tasks. First, the algorithm learns the rough gray level distribution of the lesion using a multi-region fuzzy connectedness algorithm. Second, the lesion is segmented on the current 2D plane and on 2D planes orthogonal to it using a shortest path algorithm. At the end of each segmentation, the gray level distribution for the lesion and the background is calculated and fed back into the algorithm. Finally, a random walker algorithm utilizing the seeds generated from the 2D segmentations are used to compute the 3D segmentation. Here, the algorithm determines the probability that a random walker initiating its walk from each voxel first arrives at a lesion seed before arriving at a background seed [209, 210]. The automated tracing was then manually inspected and borders were altered, as needed, using a series of manual tools. An example of a segmented nodule using this technique is illustrated in Figure 6.14.

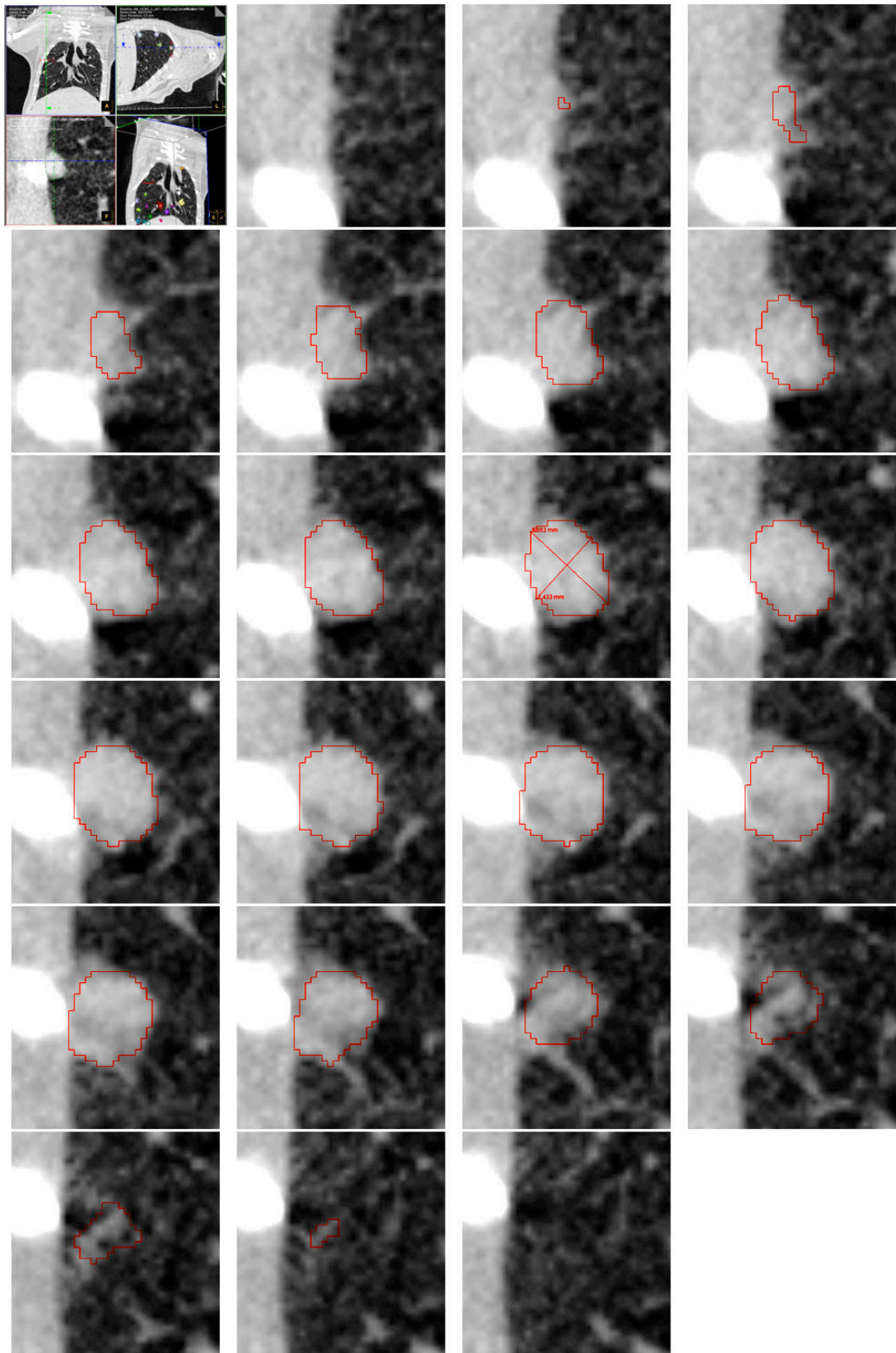


Figure 6.14: Nodule segmentation example. Top left panel represents the OncoCare segmentation software. Panels from left to right represent serial transverse serial images of the nodule with illustration of segmentation border in red.

Each tumor was given a unique label based on its lobe location: RL1 = right apical lobe, RL2= right azygous lobe, RL3 = right diaphragmatic lobe, RL4 = right cardiac lobe and LL1 = left lung, anatomical position: S = solitary, H = heart, P = pleura, L= lobe fissures, and in special cases whether a nodule was surrounded by A = atelectasis, or when a nodule had D = disappeared in a later dataset. As an example, RL3\_4\_P would represent the fourth nodule located in the right diaphragmatic lobe adjacent to the pleura.

The final longitudinal dataset for each mouse was analyzed first and followed by earlier datasets. This approach was chosen in order to label all of the nodules visible at the last time point and maintain the same labels representing the same tumors for prior scans. Identification of unique tumors across time points was performed through visual inspection of suspicious lesions with respect to anatomical landmarks such as airway bifurcations, vessels, pleural wall and lobe fissures. The dataset from the final time point, which included identified and labeled tumors, was displayed on one screen, while a prior time point was displayed on a second screen allowing fast and accurate correlation. Tumors in prior time points were labeled using their respective identifier assigned at the final time point. Tumors not present in the prior scans were given a value of zero and a marker was placed in the region where the tumor was thought to have originated for follow up inspection. Once nodules were identified using the final time point as the reference, each dataset was then reviewed for potentially new nodules that may have regressed and disappeared in the final time point.

At the completion of segmentation and labeling of each tumor across time points for each mouse, the following metrics were calculated: tumor diameter based on the Response Evaluation Criteria in Solid Tumors (RECIST) [211-213], orthogonal tumor diameter (Ortho), tumor diameter based on the World Health Organization (WHO) response criteria [211-213], 3D tumor volume, mean tumor HU density of voxels within the volume and standard deviation of HU density within each tumor volume. This data was exported and formatted for further statistical analysis using SPSS (SPSS Inc, Chicago, Illinois).

### **6.2.8.2 Micro-PET image analysis**

Micro-PET data sets were visualized in Osirix [214] and Amira (Mercury Computer Systems, Chelmsford, Massachusetts) where subjective analysis was performed on the level of FDG and FLT uptake.

### **6.2.8.3 Micro-MRI image analysis**

Micro-MRI data sets were visualized in Osirix [214] and Amira (Mercury Computer Systems, Chelmsford, Massachusetts) where identification of lung tumors was performed.

### **6.2.8.4 LSCM image analysis**

Images acquired using the LSCM technique were visualized in Image J and subjectively analyzed for tissue structure, nuclear size, shape and emission spectra.

### **6.2.8.5 LIMA image analysis**

The LIMA dataset was used as a reference when assessing the underlying pathology in the non-invasive imaging modalities. No quantitative analysis was performed on the LIMA dataset, and its primary utility was bridging the non-invasive datasets to the histology slides.

### **6.2.8.6 Histology image analysis**

Assessment of all lesions were made with the assistance of an expert lung pathologist (Dr. Jamie Weydert). Tumors were identified and classified into their respective histological sub-types as described in a recent paper by the Mouse Models for Human Cancer Consortium on pulmonary lesions [96].

## **6.2.9 Multi-Modal Registration**

A multi-step approach was taken for accurate registration of the *in vivo* and fixed *ex vivo* datasets. Registration across the imaging modalities was performed using the *ex*

*in vivo* micro-CT data set as the basis. Using this dataset as the central reference permitted the highly deformable *in vivo* micro-CT data set to be registered to a data set of the same information content, while the *ex vivo* micro-CT data set, by nature of the method of acquisition, was already well registered to the LIMA and subsequent histology slides which are of different information content. Micro-PET and micro-MRI datasets were initially registered to the *in vivo* micro-CT data set and then transformed using the same transformation matrix calculated between the *in vivo* micro-CT and *ex vivo* micro-CT datasets.

Registration between *in vivo* to *ex vivo* micro-CT datasets was performed using a non-rigid affine transformation based on mutual information. The *ex vivo* to LIMA and histology datasets were registered using a rigid correlation registration algorithm using the Amira (Mercury Computer Systems, Chelmsford, Massachusetts) imaging software package.

Initially, the lung parenchyma was segmented from either the thorax in the *in vivo* datasets, or the foam embedment in the *ex vivo* datasets. This step assisted the registration process by focusing the algorithm on the highly deformable *in vivo* lung parenchyma features such as the vessels and airways, as opposed to the rigid skeletal structure. Segmentation of the lung from the *in vivo* micro-CT dataset was performed using a region-growing algorithm based on the radio-density Hounsfield values. Segmentation of the lung from the LIMA color dataset was performed through creation of a mask via manual tracing of the lung borders. Segmentation of the *ex vivo* micro-CT and histology was not needed, as the foam did not result in enough “noise” to prevent accurate registration.

A flow diagram of the registration procedure described above is shown in Figure 6.15.

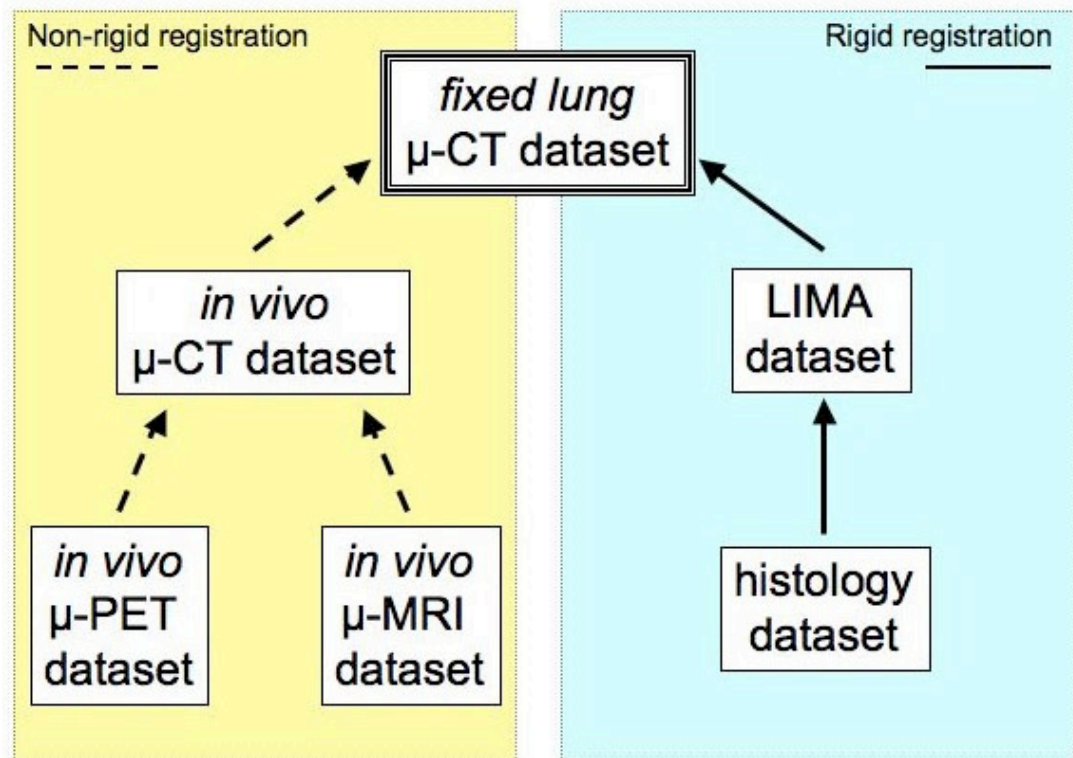


Figure 6.15: Multi-modal registration flow diagram.

Once registered, each dataset was re-sampled into the orientation of the reference dataset (*ex-vivo* micro-CT) and saved in their original file format. At this point, each dataset could be viewed individually or simultaneously with varying transparency levels allowing for direct comparisons whether subjectively through visualization or objectively using computer analysis algorithms. Also, for this study each lesion identified in the micro-CT datasets could now be accurately traced back to the histology for precise correlation.

## 6.3 Results

### 6.3.1 Micro-CT Imaging

*In-vivo* micro-CT datasets acquired from each mouse at each time point were used for non-invasive analysis of tumor growth over time. Figure 6.16 represents coronal images from one Urethane mouse lung from this study at time points 2, 3, 4 and 6 months post Urethane administration.

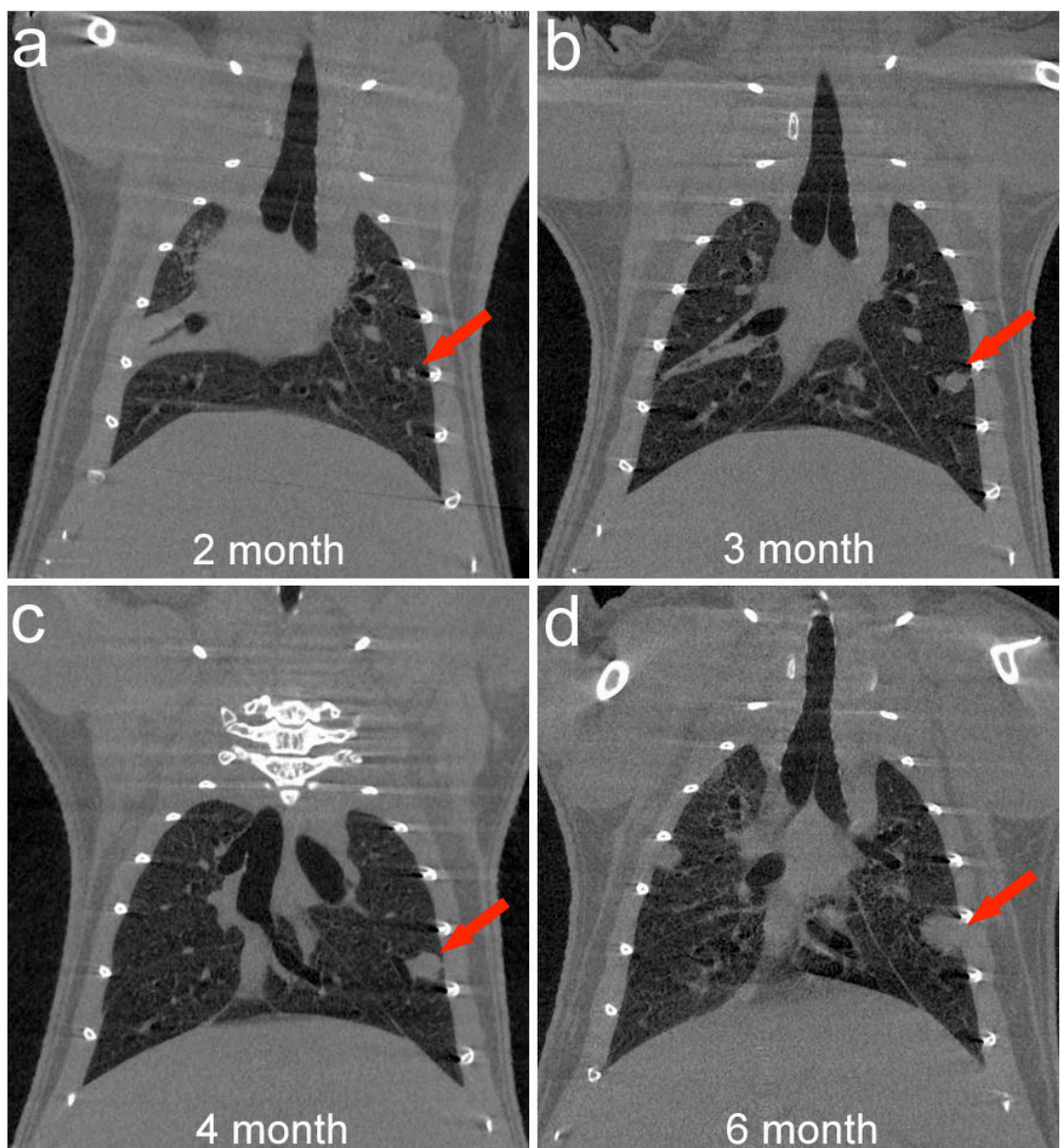


Figure 6.16: (a-d) Coronal micro-CT image from a Urethane mouse lung at 2, 3, 4 and 6-month time points. Red arrows indicate the same tumor progressing over time.

A three-dimensional reconstruction of a segmented tumor within an *in vivo* micro-CT mouse scan at the six-month time point is shown in Figure 6.17. Here, the bone (yellow), lung (pink), vessels (blue) and the tumor volume (red) have been segmented using a combination of manual and automated techniques using the Amira (Mercury Computer Systems, Chelmsford, Massachusetts) imaging software package.

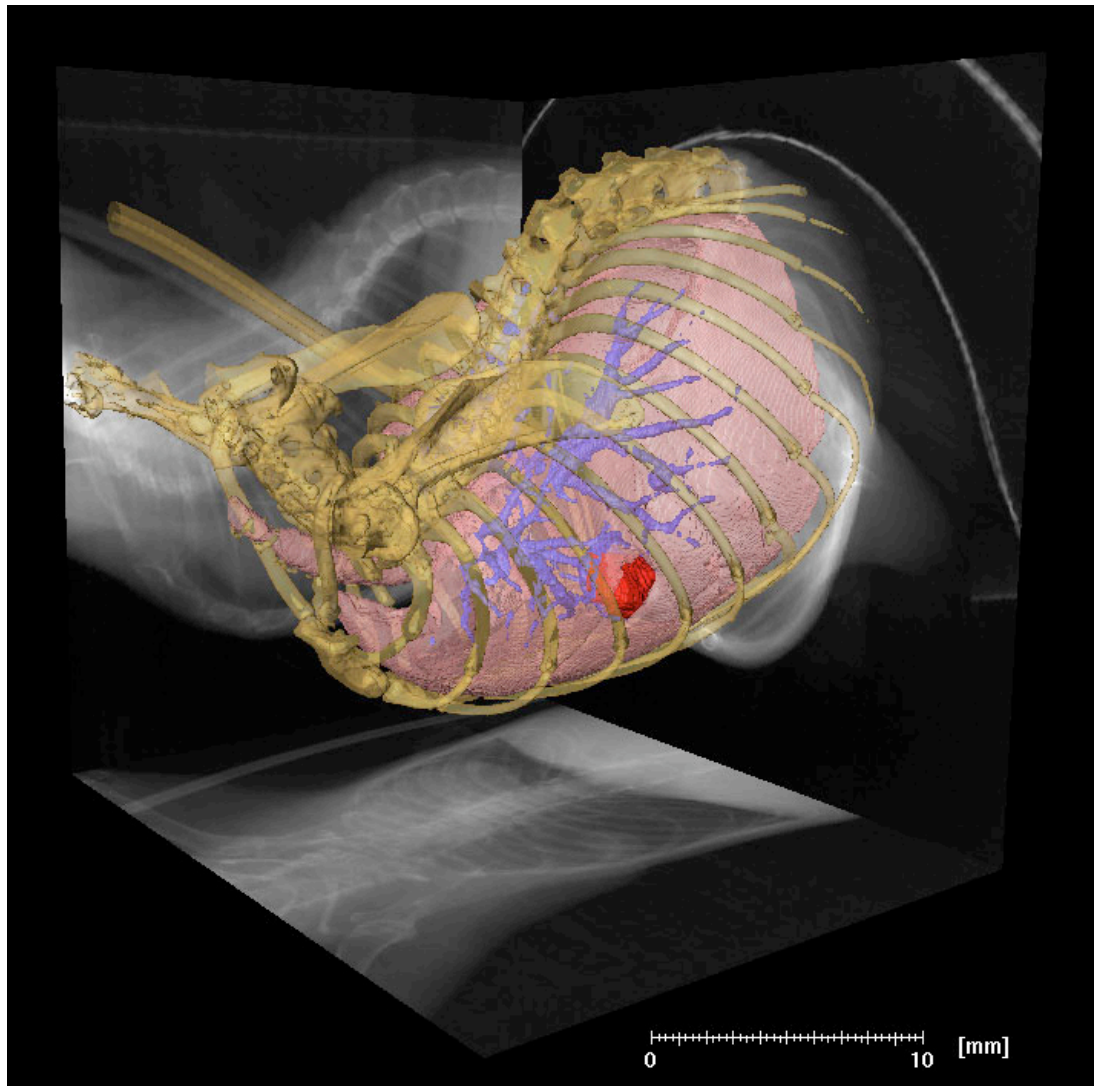


Figure 6.17: Three-dimensional reconstruction of a Urethane mouse depicting the skeletal system (yellow), lung (pink), vasculature (blue) and tumor volume (red).

In Figure 6.18 (a), a magnified view of the tumor volume and vessel structure is shown revealing the tumor extra-vasculature. Also shown in Figure 6.18 (b) is a reconstruction where the tumor shadow is clearly visible in the projected chest X-ray.

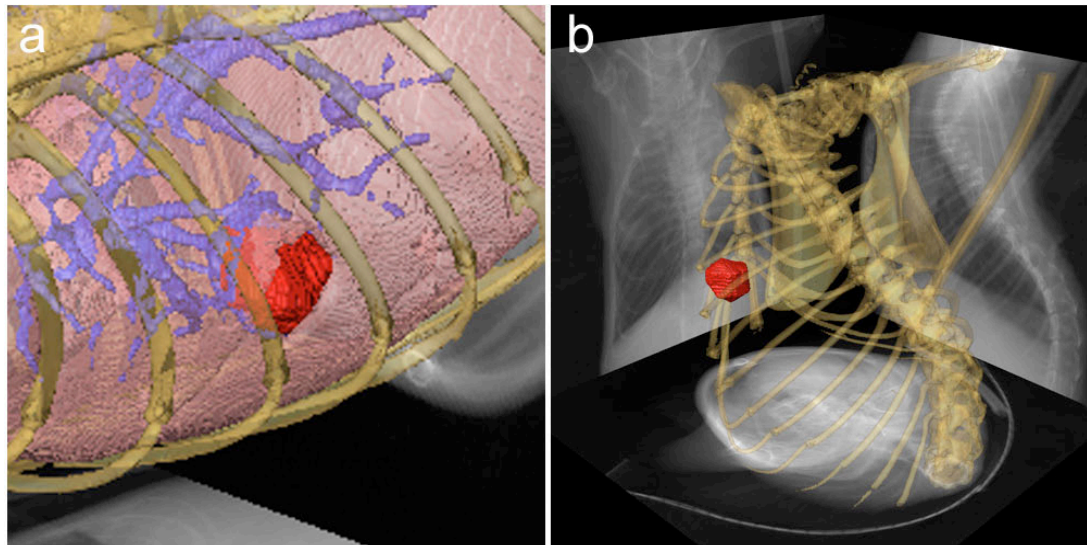


Figure 6.18: (a) magnified view of the tumor volume and surrounding vasculature, (b) tumor volume with representative projection X-rays.

A total of 794 tumor locations and 577 three-dimensional tracings were extracted from 27 micro-CT *in vivo* longitudinal datasets obtained from the first three groups of mice. 250 unique tumors were identified from the 9 mice contained therein. Using the RECIST criteria, tumors as small as 0.112mm and as large as 2.693mm were identified. Tumors with a mean of 0.721mm (+/-0.318 Std) per mouse were found over the 6-month period. A general overview of the statistics accumulated in this study is shown in Table 3.

	N	Minimum	Maximum	Mean	SEM	Std. Dev
RECIST (mm)	577	0.112	2.693	0.721	0.013	0.318
Ortho (mm)	577	0.071	1.635	0.533	0.010	0.249
WHO (mm)	577	0.008	4.302	0.456	0.018	0.434
Volume (ul)	577	0.001	5.960	0.206	0.017	0.406
HU (mean)	577	-705.513	176.104	-206.252	6.885	165.088

Table 3: Tumor Descriptive Statistics.

An example of tumor metrics extracted from lung nodules identified and tracked within a single mouse using the micro-CT datasets from this study are shown in Figure 6.19, Figure 6.20, and Figure 6.21. Here, tumor size as measured using three metrics, RECIST (mm), WHO (mm) and tumor volume ( $\mu$ l), respectively, are plotted against time (months) post Urethane administration.

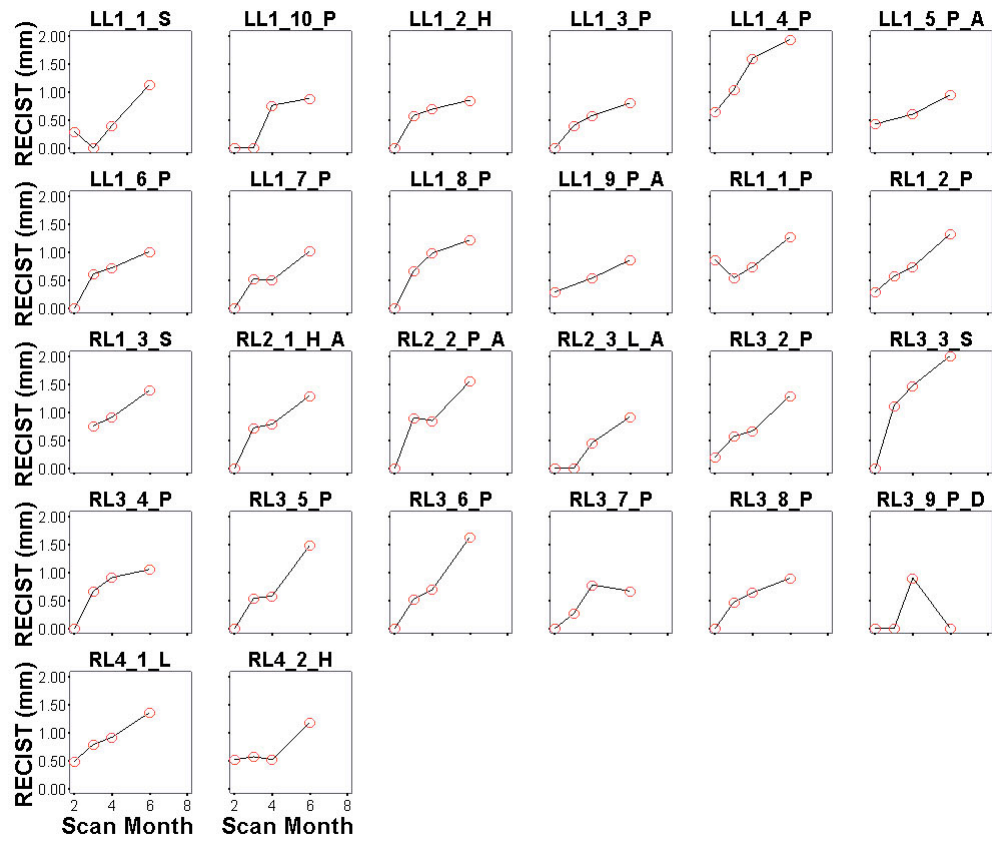


Figure 6.19: Group 3, Mouse 3, RECIST tumor size (mm) versus time for each nodule.

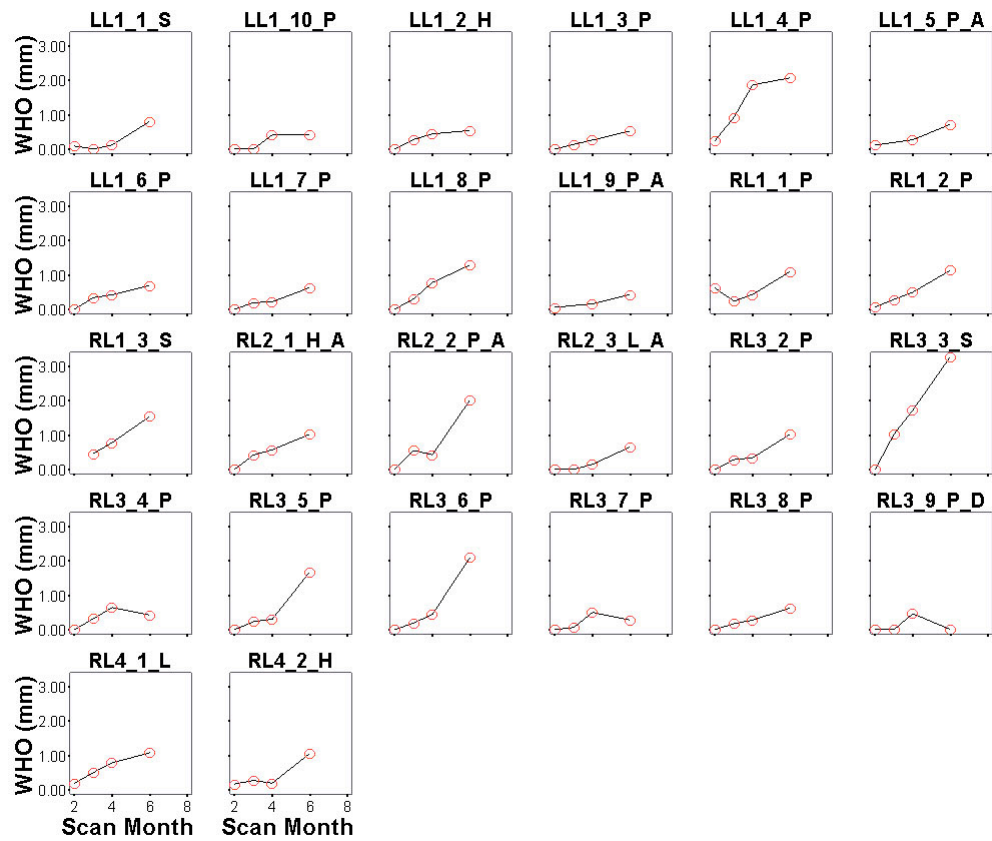


Figure 6.20: Group 3, Mouse 3, WHO tumor size (mm) versus time for each nodule.

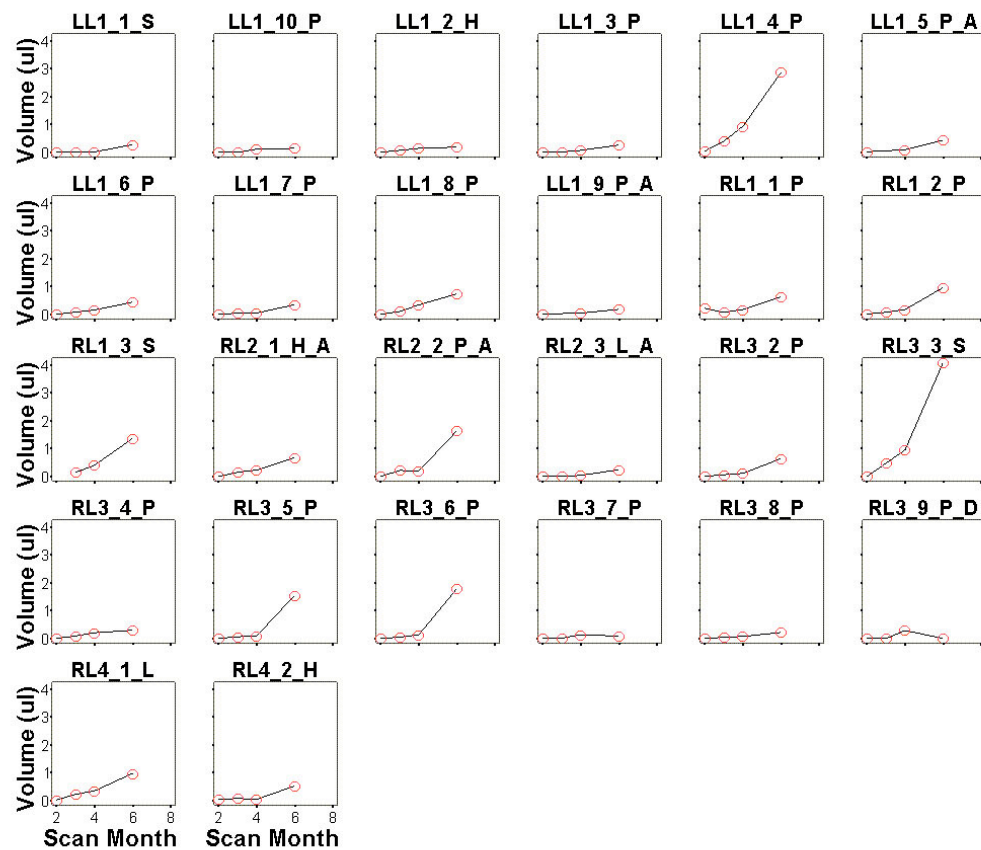


Figure 6.21: Group 3, Mouse 3, tumor volume ( $\mu\text{l}$ ) versus time for each nodule.

Longitudinal lung nodule data for each of the nine mice in this study are included in Appendix B. Here, tumor growth data for five size metrics are presented, RECIST (mm), WHO (mm), Ortho (mm), tumor volume ( $\mu\text{l}$ ), and the average Hounsfield (HU) value within the tumor volume. When the nodule cannot be identified in the initial datasets, the data point in the RECIST, WHO, Ortho and tumor volume plots, is set to zero. This does not represent an actual measurement but aids in the visualization of tumor growth.

A plot of the mean number of tumors identified at each time point after Urethane administration across all mice and within each lobe is shown in Figure 6.22.

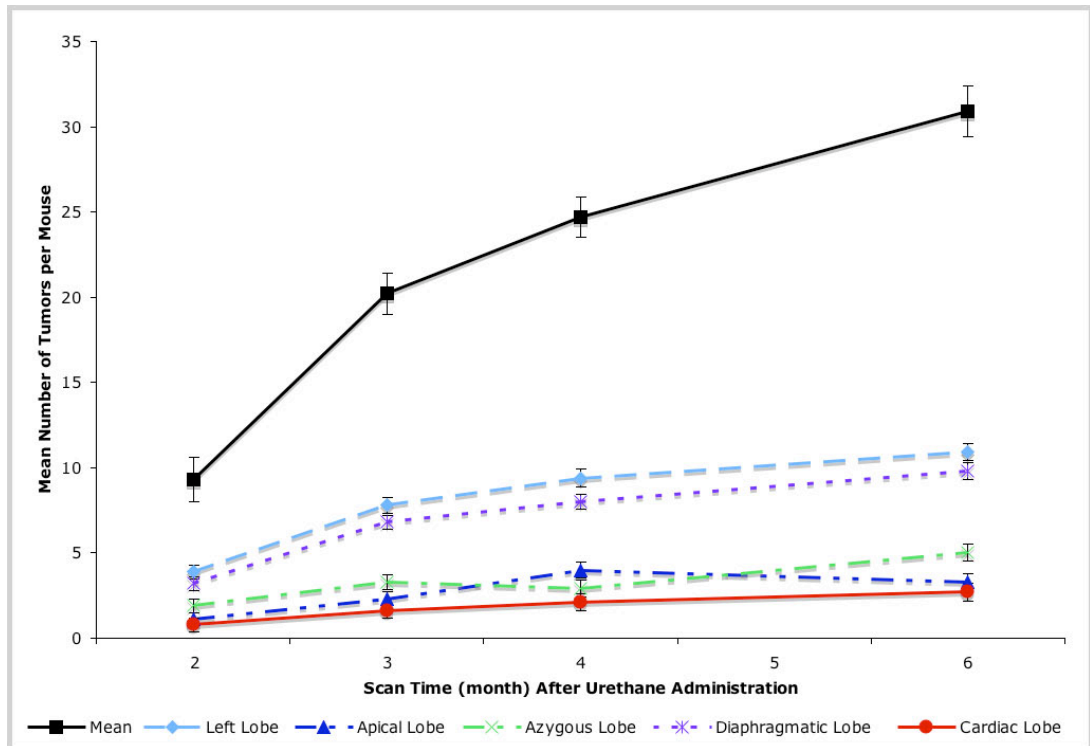


Figure 6.22: Mean number of tumors per mouse, left lung, right apical lobe, right azygous lobe, right diaphragmatic lobe and right cardiac lobe versus number of months after Urethane administration. Error bars represent the SEM.

The volume percentage of each lobe within a normal A/J mouse was calculated and tabulated in Table 4. The tumor incidence percent as calculated in this study has also been tabulated in Table 4. Figure 6.23 represents a graph of the tumor incidence percentage and lobe volume percentage versus anatomical lobe.

Lobe Frequency			
	Tumor Incidence Percent	Avg Lobe Volume Percent	Tumor to Volume Ratio
Left Lung	34	36	0.9
Apical Lobe	12.3	15	0.8
Azygous Lobe	13	13	1
Diaphragmatic Lobe	32.9	27	1.2
Cardiac Lobe	7.8	8	1

Table 4: Tumor incidence and lobe volume versus lobe location.

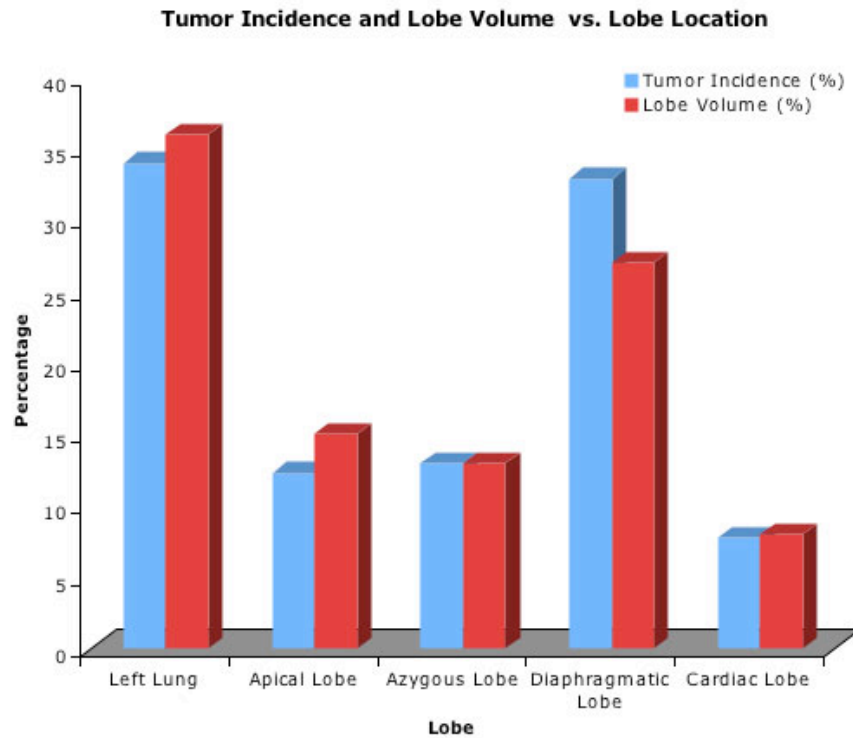


Figure 6.23: Tumor incidence and lobe volume versus lobe location.

A box plot of the mean tumor size as measured using the RECIST criteria versus time is shown in Figure 6.24. Here, the box plot represents a summary of the statistics from five common metrics. The lower whisker depicts the smallest non-outlier observation, the first quartile is represented by the bottom of the solid box, the median by the line inside the box, the second quartile by the top of the box and finally the largest non-outlier observation by the highest whisker. Mild outliers are represented by circles and extreme outliers with stars. Table 5 represents general statistics on the mean tumor size used in Figure 6.24.

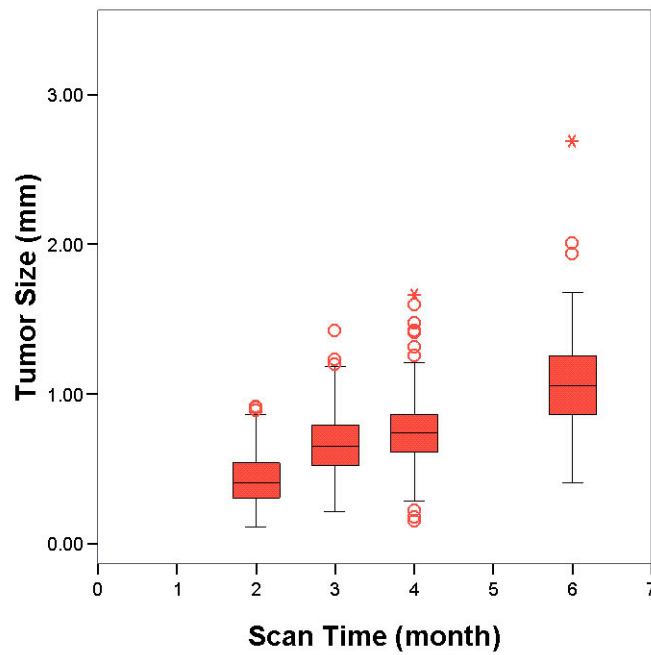


Figure 6.24: Plot of the mean tumors size measured using the RECIST criteria versus time.

Scan Time	RECIST (mm)					
	Mean	N	Std. Dev	Minimum	Maximum	SEM
Month 2	0.435	116	0.173	0.112	0.919	0.016
Month 3	0.671	195	0.230	0.212	1.430	0.016
Month 4	0.762	165	0.248	0.153	1.664	0.019
Month 6	1.068	101	0.353	0.403	2.693	0.035

Table 5: RECIST statistics for lung tumors versus scan time.

A box plot of the mean tumor size as measured using the RECIST criteria versus lobe location is shown in Figure 6.25. Table 6 represents general statistics on the mean tumor size versus lobe location used in Figure 6.25.

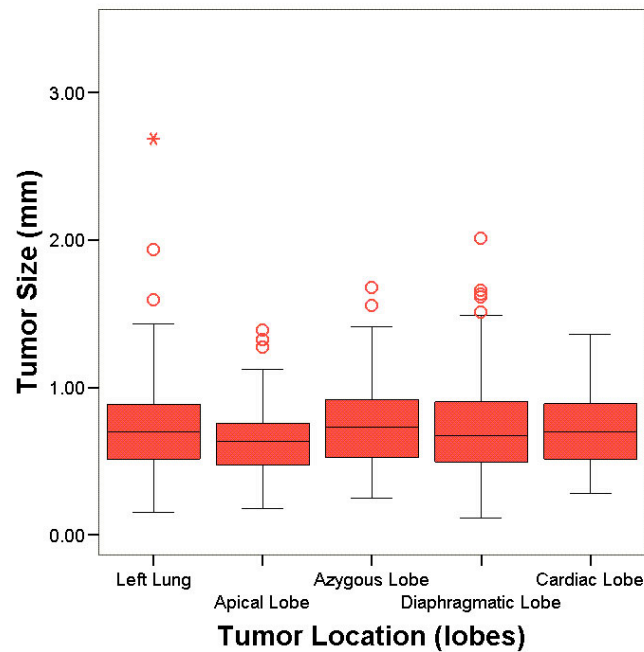


Figure 6.25: Plot of the mean tumors size measured using the RECIST criteria versus lobe location.

Lobe	RECIST (mm)					
	Mean	N	Std. Dev	Minimum	Maximum	SEM
Left Lung	0.730	196	0.328	0.153	2.693	0.023
Apical Lobe	0.633	71	0.260	0.180	1.395	0.031
Azygous Lobe	0.750	75	0.302	0.250	1.681	0.035
Diaphragmatic	0.730	190	0.340	0.112	2.013	0.025
Cardiac Lobe	0.710	45	0.290	0.283	1.360	0.043

Table 6: RECIST statistics of tumor size versus anatomical lobes.

A box plot of the mean tumor size as measured using the RECIST criteria versus time for each lobe location is shown in Figure 6.26. Table 7 represents general statistics on the mean tumor size versus time for each lobe location used in Figure 6.26.

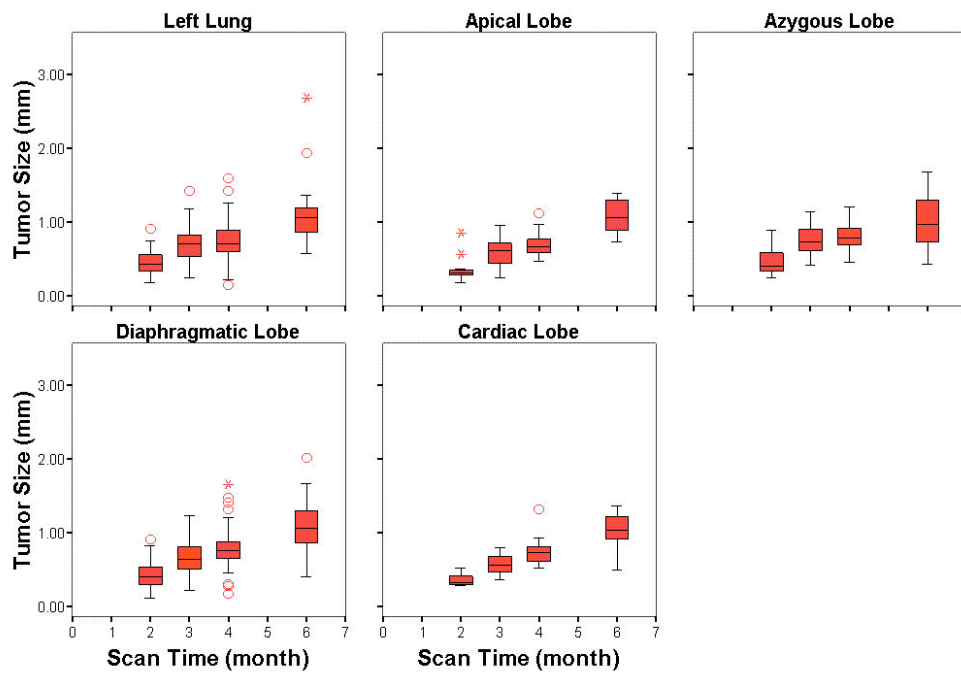


Figure 6.26: Plot of the mean tumors size measured using the RECIST criteria versus time for each lobe.

Lobe	Scan Time	RECIST (mm)						
		Mean	N	Std. Dev	Minimum	Maximum	SEM	
Left Lung	Month 2	0.451	41	0.156	0.180	0.919	0.024	
	Month 3	0.699	66	0.238	0.250	1.430	0.029	
	Month 4	0.745	53	0.263	0.153	1.601	0.036	
	Month 6	1.084	36	0.375	0.570	2.693	0.062	
Apical Lobe	Month 2	0.363	12	0.182	0.180	0.860	0.052	
	Month 3	0.579	28	0.185	0.250	0.961	0.035	
	Month 4	0.701	24	0.158	0.472	1.124	0.032	
	Month 6	1.082	7	0.263	0.728	1.395	0.099	
Azygous Lobe	Month 2	0.482	18	0.210	0.250	0.894	0.049	
	Month 3	0.752	26	0.199	0.412	1.140	0.039	
	Month 4	0.822	17	0.215	0.461	1.210	0.052	
	Month 6	1.002	14	0.391	0.427	1.681	0.105	
Diaphragmatic Lobe	Month 2	0.433	38	0.175	0.112	0.912	0.028	
	Month 3	0.669	63	0.250	0.212	1.235	0.031	
	Month 4	0.787	56	0.283	0.180	1.664	0.038	
	Month 6	1.090	33	0.371	0.403	2.013	0.064	
Cardiac Lobe	Month 2	0.362	7	0.101	0.283	0.522	0.038	
	Month 3	0.566	12	0.130	0.361	0.791	0.038	
	Month 4	0.755	15	0.198	0.522	1.321	0.051	
	Month 6	1.027	11	0.258	0.500	1.360	0.078	

Table 7: RECIST statistics for each lobe at each time point.

A percentage histogram of the mean tumor size is shown in Figure 6.27.

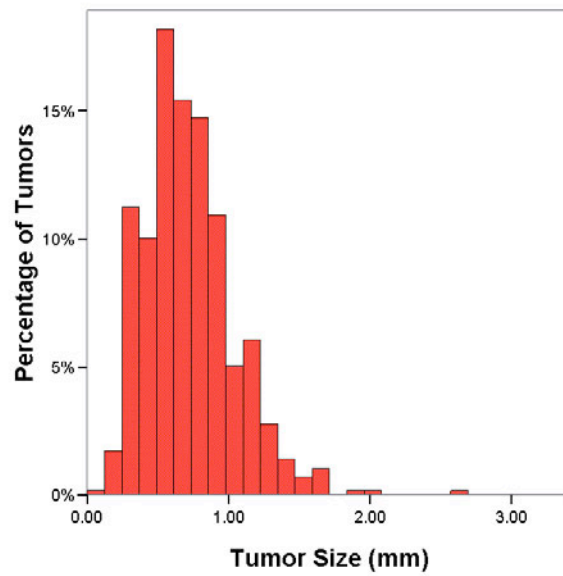


Figure 6.27: Percentage histogram for the mean tumor size measured using the RECIST criteria.

The percentage histogram of the mean tumor size for each lobe is shown in Figure 6.28.

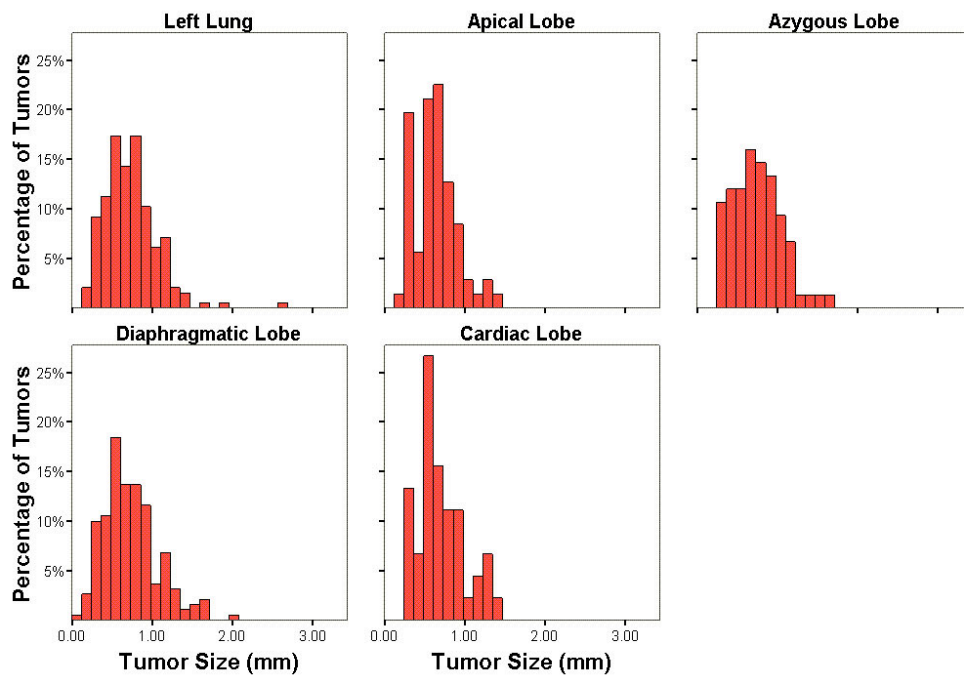


Figure 6.28: Percentage histogram for the mean tumor size measured using the RECIST criteria for each lobe.

The percentage histogram of the mean tumor size at each time point is shown in Figure 6.29.

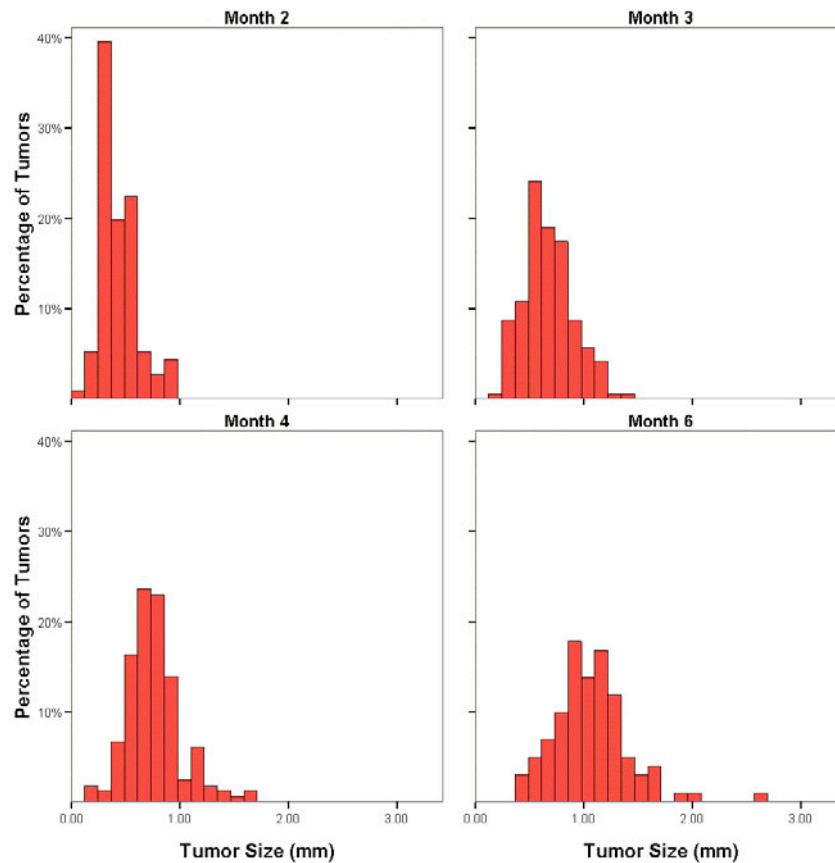


Figure 6.29: Percentage histogram for the mean tumor size measured using the RECIST criteria at each time point.

Statistical significance was calculated using a test of Fixed Effects, a linear mixed-effect model that enables simultaneous sampling of normally distributed data to extract effects that affect the population mean (fixed effect) from random subject effects (random effect). Here, the number of identified nodules was analyzed and a significant lobe-time interaction ( $p=0.003$ ) was found. Pair wise comparison between lobes at each time revealed that at 3, 4 and 6 months, the mean number of nodules in the left lung is significantly greater than the apical ( $p=0.003$ ,  $p=0.010$ ,  $p=0.0007$ ), azygous ( $p=0.031$ ,  $p=0.001$ ,  $p=0.014$ ), and cardiac lobe ( $p=0.001$ ,  $p=0.0005$ ,  $p=0.0004$ ). The diaphragmatic lobe shows a similar significance when

compared to the apical, azygous and cardiac lobes. No significant interaction was found between the left lung and diaphragmatic lobe.

Using a test of Fixed Effects on the RECIST data, normalized to the body weight at each scan point, revealed no significant lobe-time interaction ( $p=0.143$ ) indicating parallel RECIST growth profiles over time among lobes. This result in conjunction with the strong relationship between tumor number and lobe size indicates that on average tumor growth is similar across lobes. In contrast, when performing the same test on the WHO data, there is a suggested lobe-time interaction ( $p=0.056$ ), indicating non-parallel WHO growth profiles over time within lobes. In particular, the growth profile between the apical and azygous lobe showed a non-parallel growth rate ( $p=0.012$ ), where between month 3 and 4 the apical lobe had a mean increase in WHO compared to the azygous lobe (3.7 times vs. 1.6 times;  $p=0.030$ ).

Further analysis performed on the tumor Volume data using a test of Fixed Effects resulted in a significant lobe-time interaction ( $p=0.027$ ) indicating non-parallel volume growth profiles over time among the lobes. Comparing tumor growth profiles between lobes showed non-parallel growth profiles between the apical and azygous lobe ( $p=0.002$ ) and between the apical and diaphragmatic lobe ( $p=0.031$ ). Pair wise comparisons between lobes showed a significantly lower mean tumor volume at 3 months for the apical lobe when compared to the azygous ( $p=0.002$ ) and diaphragmatic lobe ( $p=0.024$ ). This was also similarly observed when comparing the apical with the left lobe, but was not significant at the 0.05 significance level ( $p=0.084$ ). No significant difference in mean tumor volumes was observed among all lobes at month 2, 4 and 6 ( $p>0.99$ ). Between month 3 and 4, the apical lobe showed a significantly greater mean increase in tumor volume (6.7 times) when compared to the azygous (2.0 times;  $p=0.003$ ) and diaphragmatic (2.8 times;  $p=0.039$ ). This was also similarly observed when comparing the apical with the left lobe (2.3 times;  $p=0.084$  but was not significant at the 0.05 significance level).

Figure 6.30 represents an illustration of a nodule from a mouse in this study, identified in an earlier scan, that regressed and was not visible in final scan.

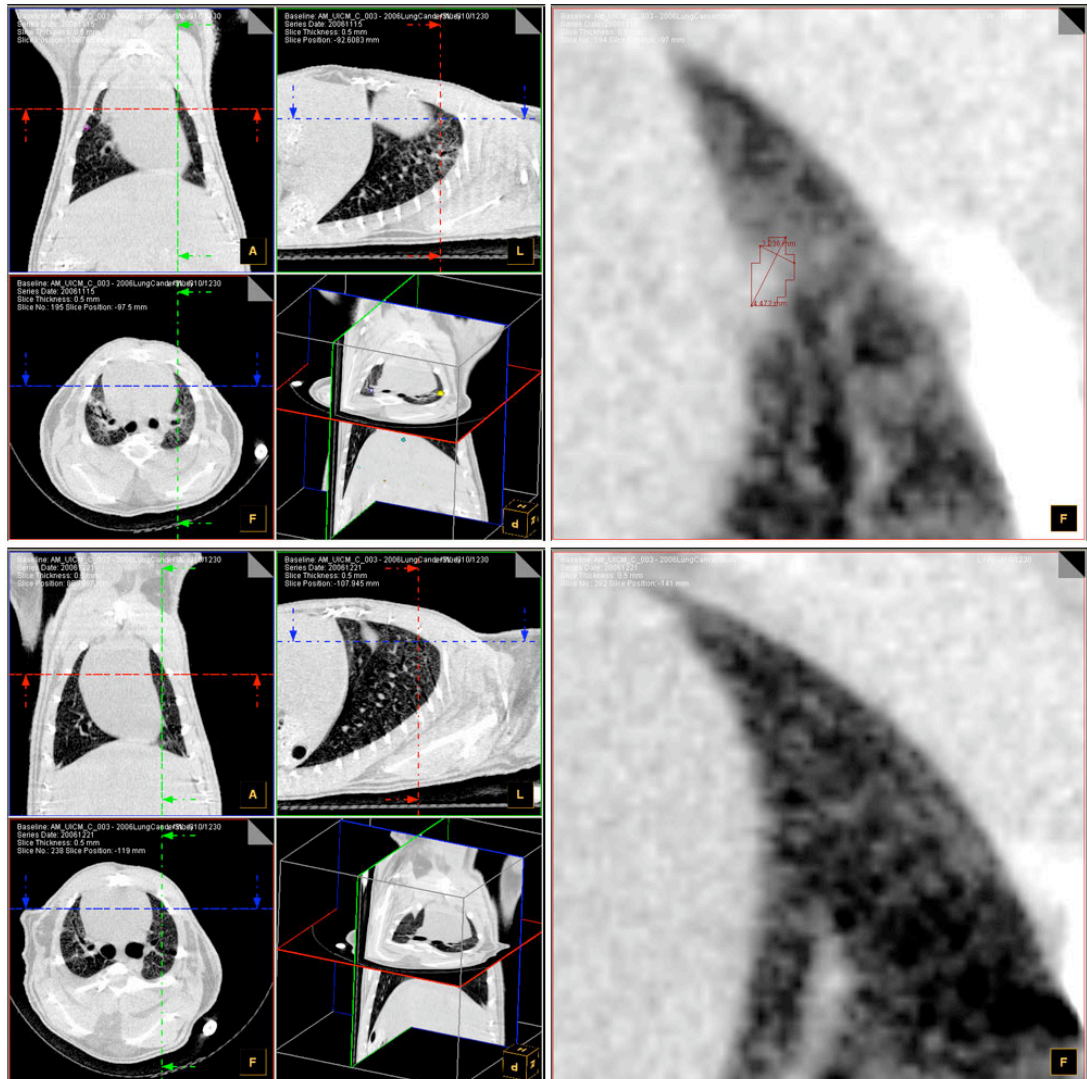


Figure 6.30: Disappearing nodule illustration. (a-b) represents the identified nodule at month 2, and (c-d) represents the same region post registration with no nodule. (a) and (c) represent screen shot from Siemens OncoCare nodule segmentation package, and (b) and (d) represents a magnified image of the appropriate transverse slice from the bottom left sub-image of each time point.

## 6.3.2 PET and MRI Imaging

### 6.3.2.1 PET Imaging

PET imaging was performed on three mice in this study at the 6-month period. A PET scan from a mouse in the 6-month group is shown in Figure 6.31 (a). Here, we can see that the heart, kidney and bladder have high uptake of the  $^{18}\text{F}$ -FDG, which is commonly observed in normal subjects, while no prominent hot spots were seen in the lung region.

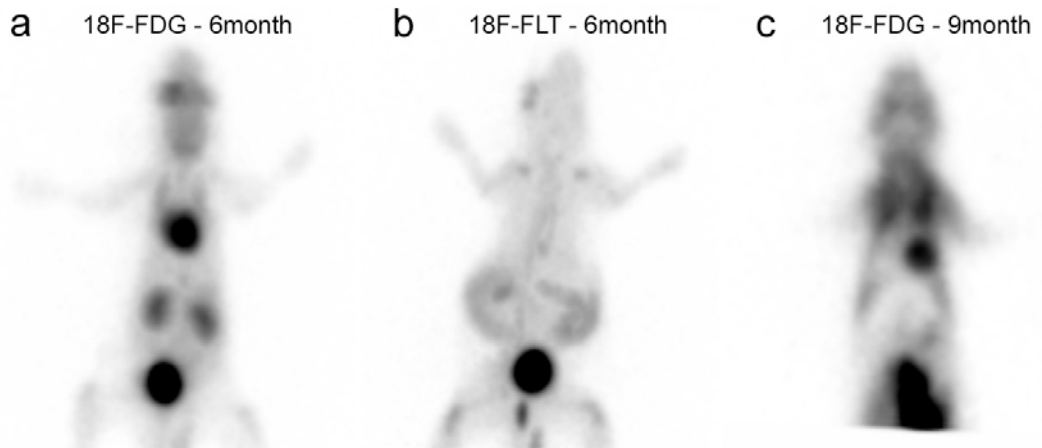


Figure 6.31: (a) 18F-FDG PET scan of a Urethane mouse at the 6-month time point, (b) 18F-FLT PET scan of the same mouse at the same time point, and (c) 18F-FDG PET scan of the same mouse at the 9-month time point. Window and level are constant across images.

An 18F-FLT scan was also performed at this time-point to determine if the sensitivity of the cell proliferation index was greater than that of FDG metabolism. Again the scan came up negative in the pulmonary region as shown in Figure 6.31 (b).

In order to determine when or if PET activity could be detected in this mouse lung cancer model, the same mouse represented in Figure 6.31 (a) & (b) was re-scanned at the 9-month time point, as shown in Figure 6.31 (c). A significant uptake of FDG is visible here in both the left and right lung. Also clearly visible is the dramatic shift of the heart towards the abdomen a result of the enlarging diaphragmatic lobe.

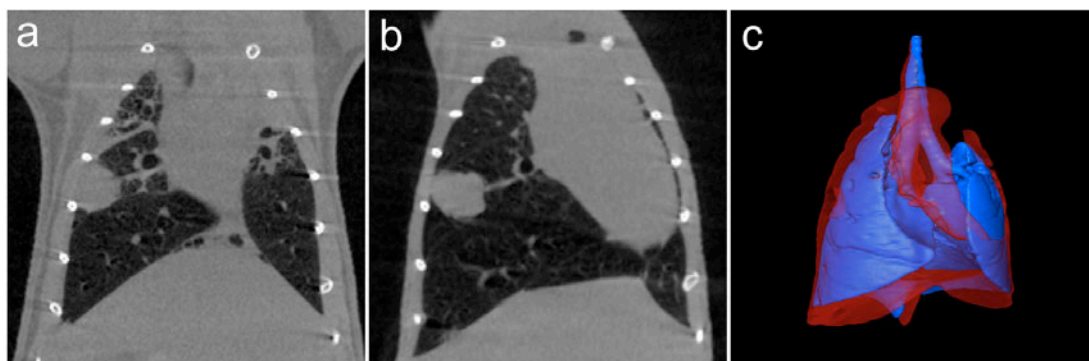


Figure 6.32: Registered micro-CT lung dataset from the same mouse shown in Figure 6.31 at 6 and 9 months in (a) and (b), respectively. (c) Illustrates the 3D reconstruction of the lung volume at 6 (blue) and 9 (red) months. Clearly the lung volume has significantly increased.

Figure 6.32 (a) & (b) represents the registered micro-CT scan for the mouse shown in Figure 6.31 (a) & (c) at months 6 and 9, respectively. From the quantitative analysis we find that the increase in the combined tumor volume between these two time points ( $10.8 \rightarrow 20.1 \mu\text{l}$ ) does not account for the increase in the lung volume ( $805 \mu\text{l} \rightarrow 1301 \mu\text{l}$ ). Figure 6.32 (c) represents a 3D reconstruction of both these lungs; here, the dramatic increase in lung volume between the 6 month (blue) and 9 month (red) is evident.

### 6.3.2.2 MRI Imaging

At the 6-month time point, three mice underwent MRI imaging in order to determine the utility of small animal MRI in detecting and potentially differentiating lung tumors. Figure 6.33 (a) represents a transverse thoracic image from a micro-CT scan and Figure 6.33 (b) a respective micro-MRI scan from the same mouse.

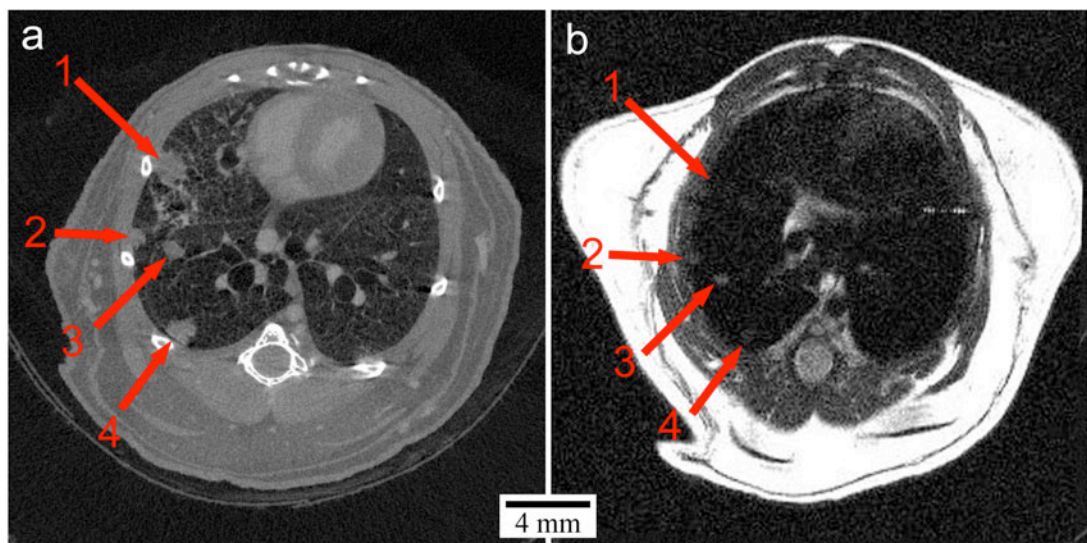


Figure 6.33: Transverse thoracic image of the same Urethane mouse using the (a) micro-CT and (b) micro-MRI system, respectively (scans acquired one day after another). As seen tumors indicated and labeled 2, 3 and 4 are visible in both the micro-CT and micro-MRI image, while nodule 1 is only visible in the micro-CT image.

### 6.3.3 CBCM and LSCM Imaging

To qualitatively evaluate the lung in the normal and Urethane mouse using confocal microscopy techniques, CBCM imaging was performed on mice lungs at the final end point prior to excision of lungs for Heitzman fixation. Figure 6.34 represents

images acquired using the CBCM technique on a normal A/J mouse (a) and a Urethane mouse (b-d). In this example, both mice had been systemically injected with Fluorescein and topically stained with 0.5mg/ml Acridine Orange. Figure 6.34 (a) represents a normal region of the lung parenchyma from the normal A/J mouse, (b) represents an image from a normal region of the lung parenchyma from the Urethane A/J mouse, (c) represents a suspicious region of the parenchyma from the Urethane A/J mouse and (d) represents a region over a large peripheral tumor from the Urethane A/J mouse. The suspicious and tumor region was defined through gross pathological observation over the exterior of the visible lung parenchyma.

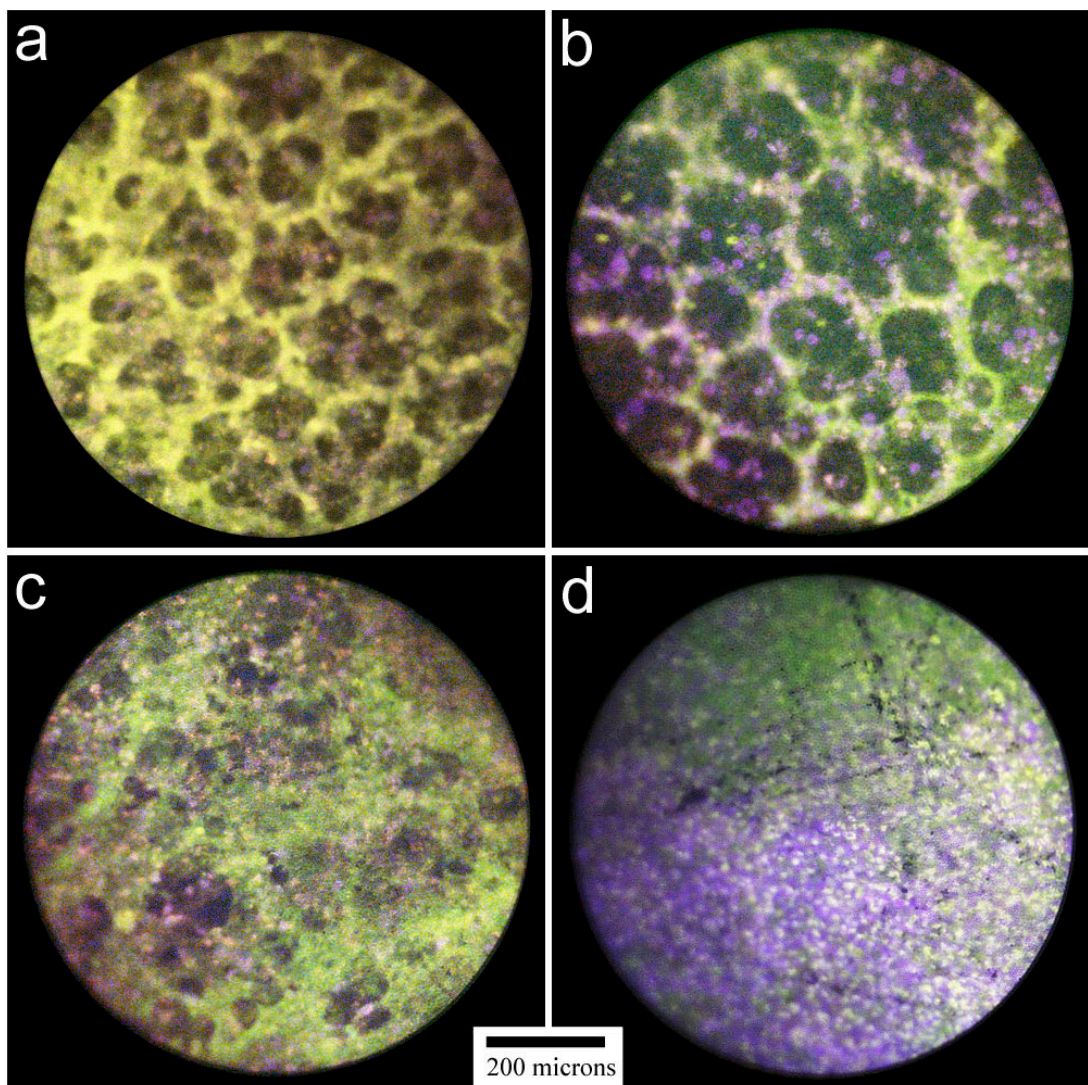


Figure 6.34: CBCM images from (a) normal A/J mouse and (b-d) Urethane mouse lung at the 6-month time point, (a) non-suspicious region from normal A/J mouse, (b) non-suspicious region from Urethane mouse (c) suspicious alveolar region from Urethane mouse, (d) large peripheral tumor from Urethane mouse.

At the completion of the CBCM imaging, select mouse lungs were placed in the LSCM imaging chamber, described in Section 5.2.

Figure 6.35 represents an example using the LSCM chamber imaging on both a normal A/J and Urethane mouse lung; here, Fluorescein and Acridine Orange stains were also used. Acridine Orange, as discussed in Section 6.2.6.4, emits green fluorescence when bound to double stranded DNA (dsDNA) and red fluorescence when bound to single stranded DNA (ssDNA). In this example, the distinction of the Acridine Orange stain bound to dsDNA (green) vs. ssDNA (blue) is clearly evident; images have been pseudo-colored using the RGB scheme outlined in Section 6.2.6.4.

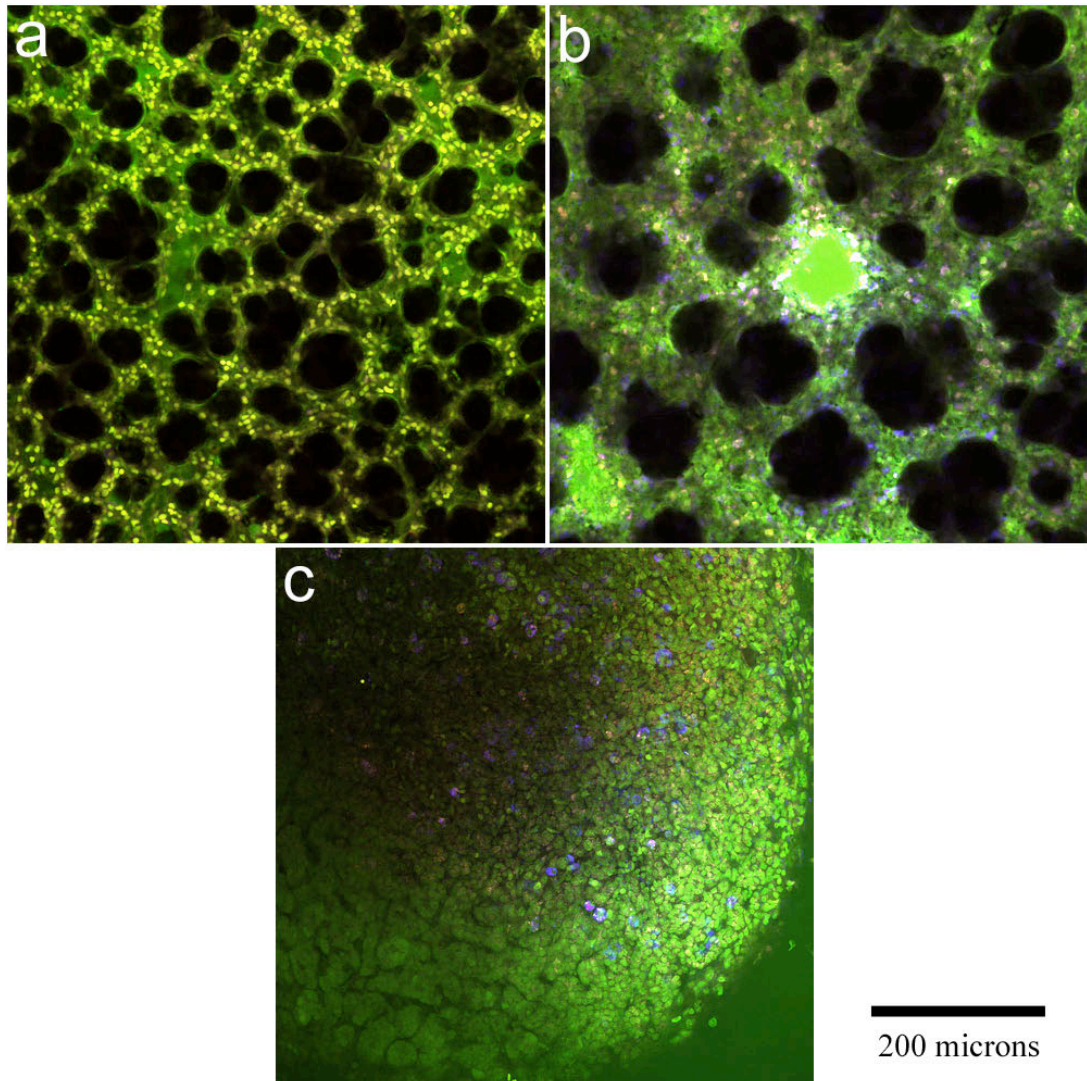


Figure 6.35: LSCM images from a normal A/J and a Urethane mouse lung at 6-months using the custom imaging chamber, (a) normal A/J mouse lung parenchyma, (b) 'normal' parenchyma from a Urethane mouse lung surrounding a micro adenoma and (c) tumor region from Urethane mouse lung. Image scale consistent across tiled examples.

Figure 6.36 represents a low magnification (4x objective) image of a tumor from a Urethane mouse at 6-months using Fluorescein and Acridine Orange as described for the examples in Figure 6.34 & Figure 6.35. Here, a nodule at the base of the left lung has been imaged with clear depiction of the tumor boundary and surrounding alveolar parenchyma.

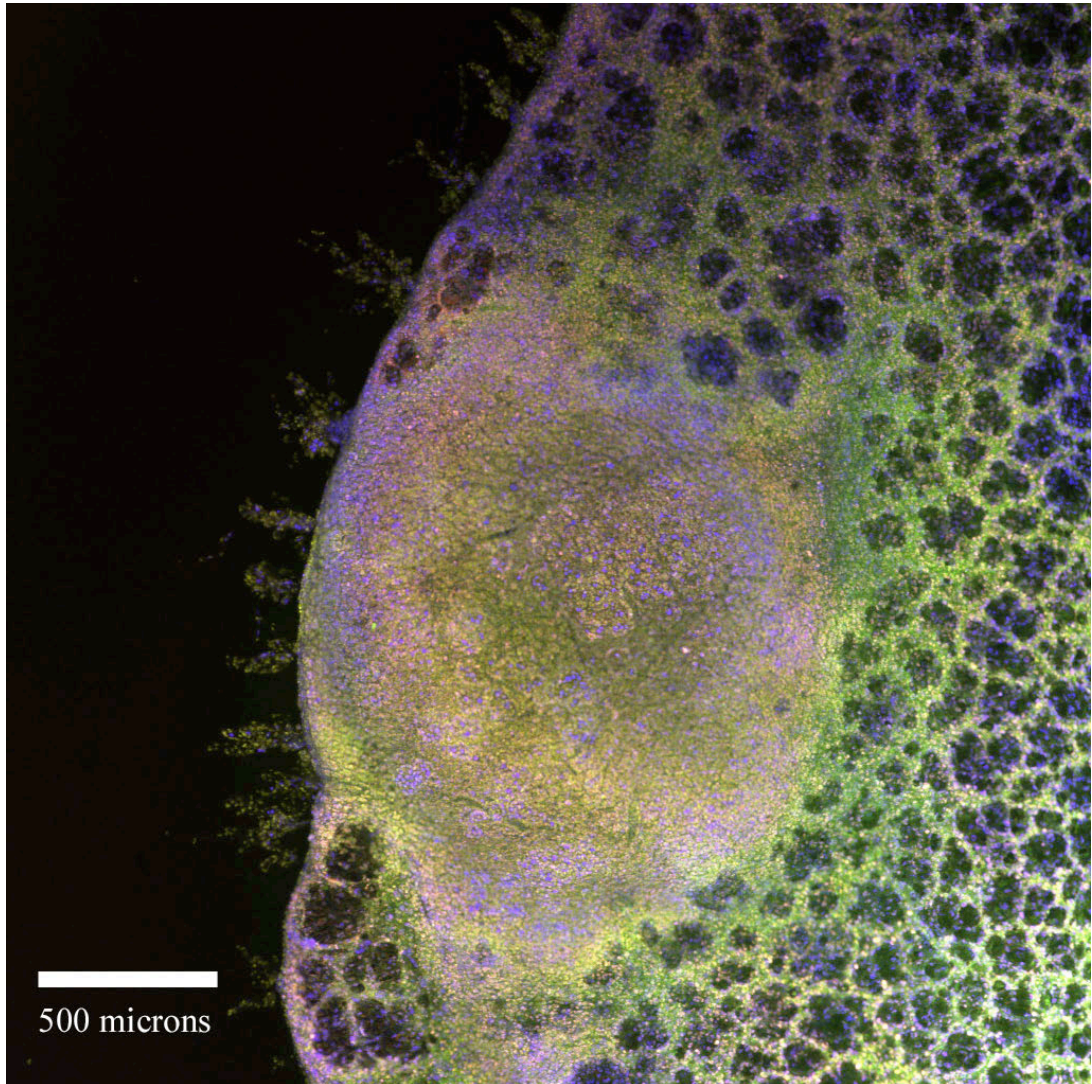


Figure 6.36: Low magnification (4x objective) LSCM image of a tumor from a Urethane mouse at 6-months. Tumor located at the base of the left lung.

In a different example LSCM, images were acquired from normal and tumor regions at high magnification. Figure 6.37 illustrates two images, where (a) represents normal parenchyma from the Urethane mouse and (b) represents the central region of a sub-pleural tumor in the same lung. In this example, the mouse had been systemically administered with Fluorescein and PKH-26 as described in Section 6.2.6.4. The imaging region of interest was also topically stained with Draq5 and Acridine Orange nuclear stain. Two nuclear stains were used in this example to take advantage of their different affinities for double and single stranded DNA; Acridine Orange has a strong affinity for both dsDNA and ssDNA, while Draq5 predominantly binds to dsDNA. Acridine Orange also emits a unique emission spectra for each type of bond.

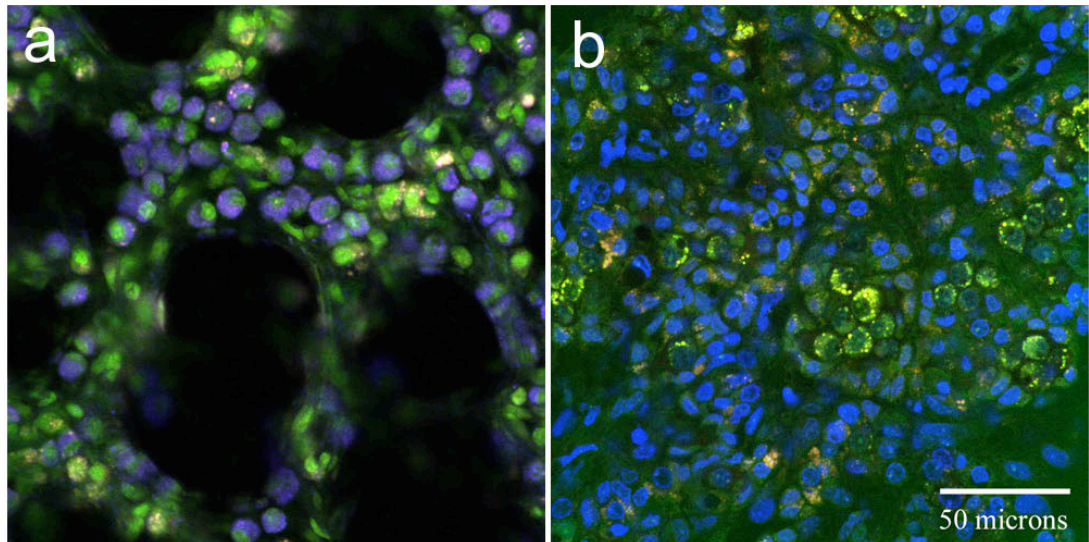


Figure 6.37: LSCM images from a Urethane mouse lung at 6-months using the custom imaging chamber, (a) normal alveolar tissue, (b) tumor tissue. Image scale consistent across examples.

Finally, Figure 6.38 represents an example with prominent PKH26-PCL alveolar macrophage labeling. Here, images were acquired between a tumor in the azygous lobe and normal parenchyma in the adjacent diaphragmatic lobe. Clearly, there are many more alveolar macrophages present in the tumor tissue than the ‘normal’ alveolar parenchyma.

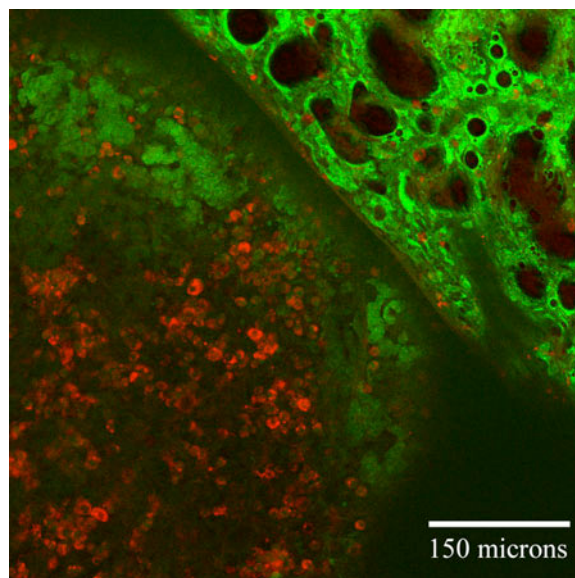


Figure 6.38: Urethane mouse lung tumor at 6-months, imaged using the LSCM imaging chamber technique with PKH26-PCL macrophage labeling.

### 6.3.4 LIMA Imaging

At the completion of the LSCM imaging, mice lungs were fixed using the Heitzman technique detailed in Section 3.2.7 and embedded in foam as detailed in Section 6.2.6.5. Embedded lungs were then imaged using the micro-CT scanner and further imaged with the LIMA system as detailed in Section 6.2.6.5. An example of a Heitzman fixed, foam embedded, Urethane mouse lung micro-CT, LIMA and Histology dataset is shown in Figure 6.39, Figure 6.40 and Figure 6.41, respectively.

The *ex vivo* micro-CT scan contained 1024 slices of which approximately 700 included the fixed lung from apex to base. Figure 6.39 represents one subset of the micro-CT dataset for a whole Urethane mouse lung. Here, 28-micron thick slices have been shown every seventeen to eighteen slices. The slices in Figure 6.39 have been chosen based on the complete LIMA dataset for the same lung, shown in Figure 6.40. Here, each LIMA image represents the top surface of the embedded lung prior to each 500-micron section. Slices removed from the LIMA system are then further processed for H&E histology. The representative histology for both the LIMA and micro-CT dataset shown in Figure 6.39 and Figure 6.40, respectively, is shown in Figure 6.41.

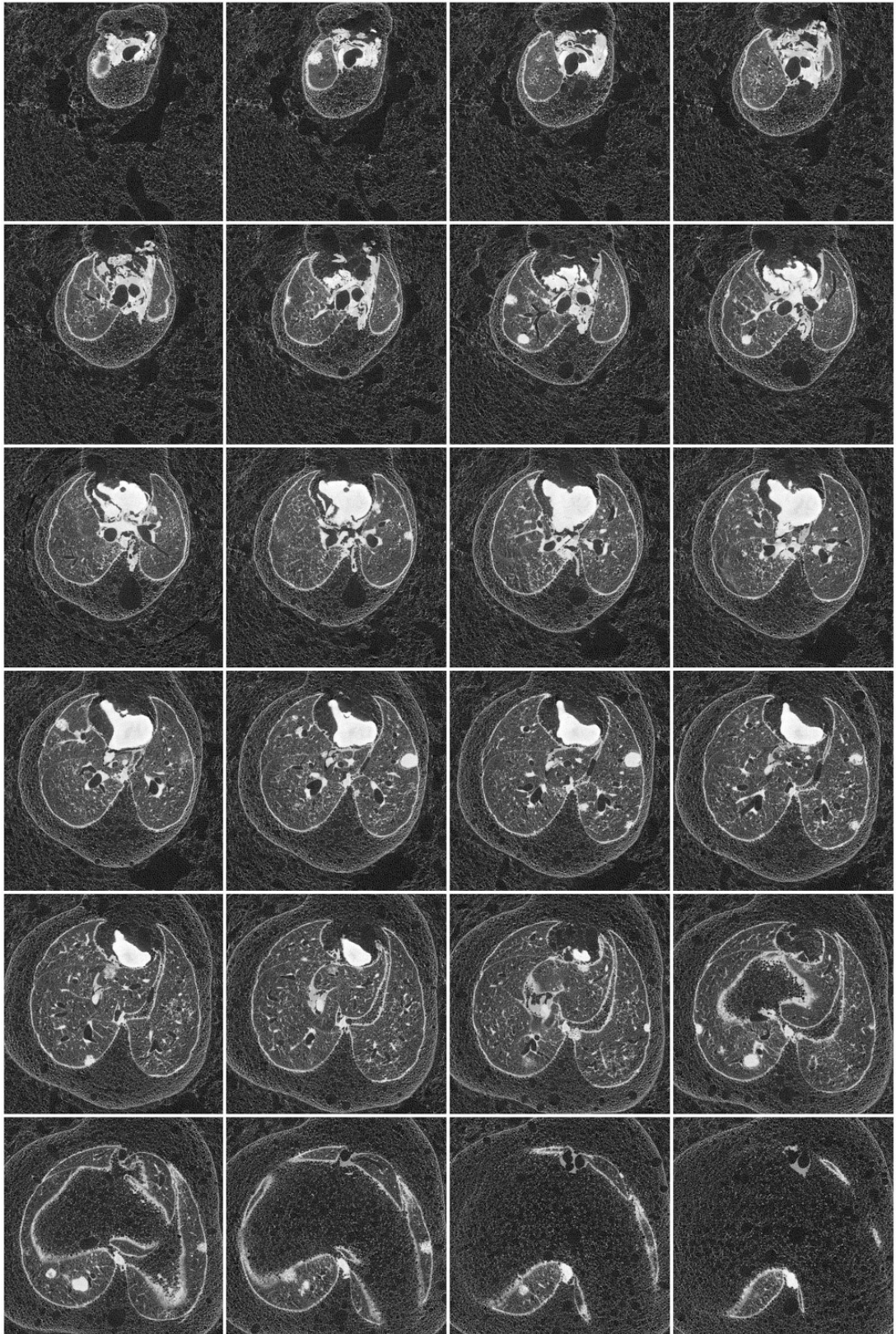


Figure 6.39: Heitzman fixed, foam embedded Urethane mouse lung micro-CT dataset. 24 images with 28 microns thickness and 500 micron spacing between images are shown from the apex to base of the lung, top to bottom, left to right respectively.

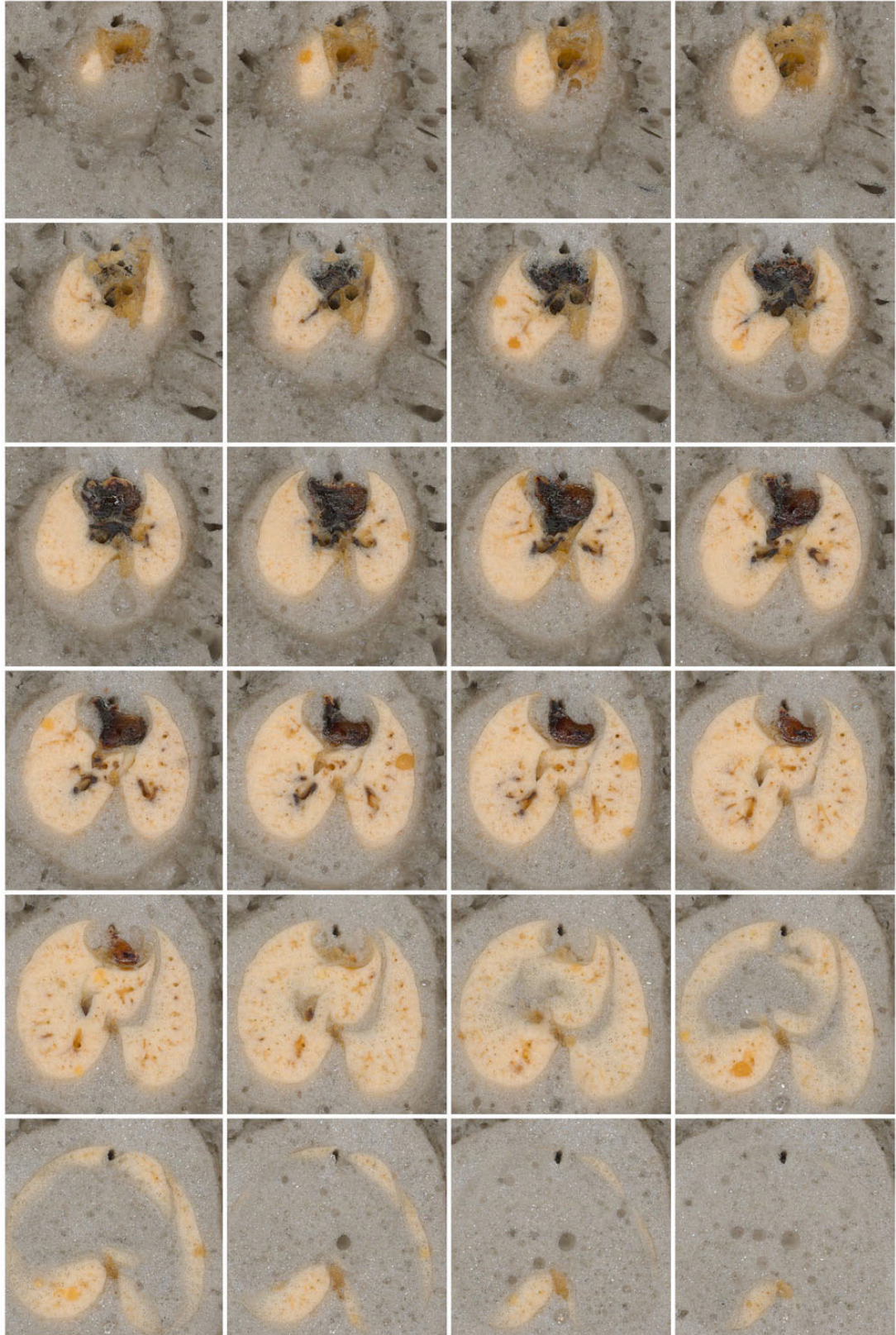


Figure 6.40: Heitzman fixed, foam embedded Urethane mouse lung LIMA complete dataset. Each tile represents an en bloc image acquired prior to a 500 micron section from the apex to base of the lung, top to bottom, left to right respectively.

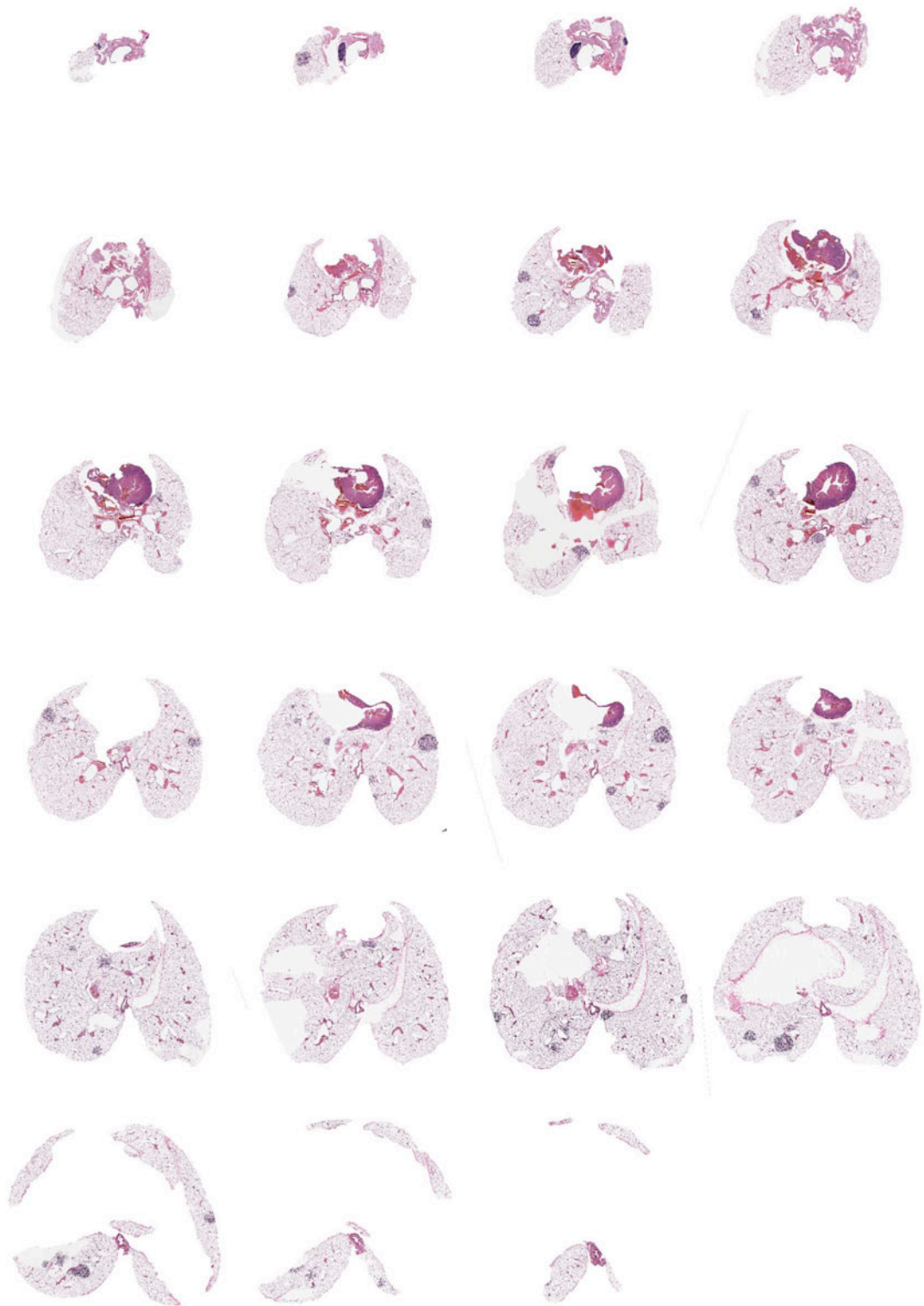


Figure 6.41: Heitzman fixed, foam embedded Urethane mouse lung H&E Histology dataset. Each tile represents a 5 micron thick section from the respective 500 micron LIMA section from the apex to base of the lung, top to bottom, left to right respectively.

Datasets were then registered as described in Section 6.2.9. An example of an *in vivo* micro-CT, *ex-vivo* micro-CT, LIMA and Histology registered dataset is shown in Figure 6.42.

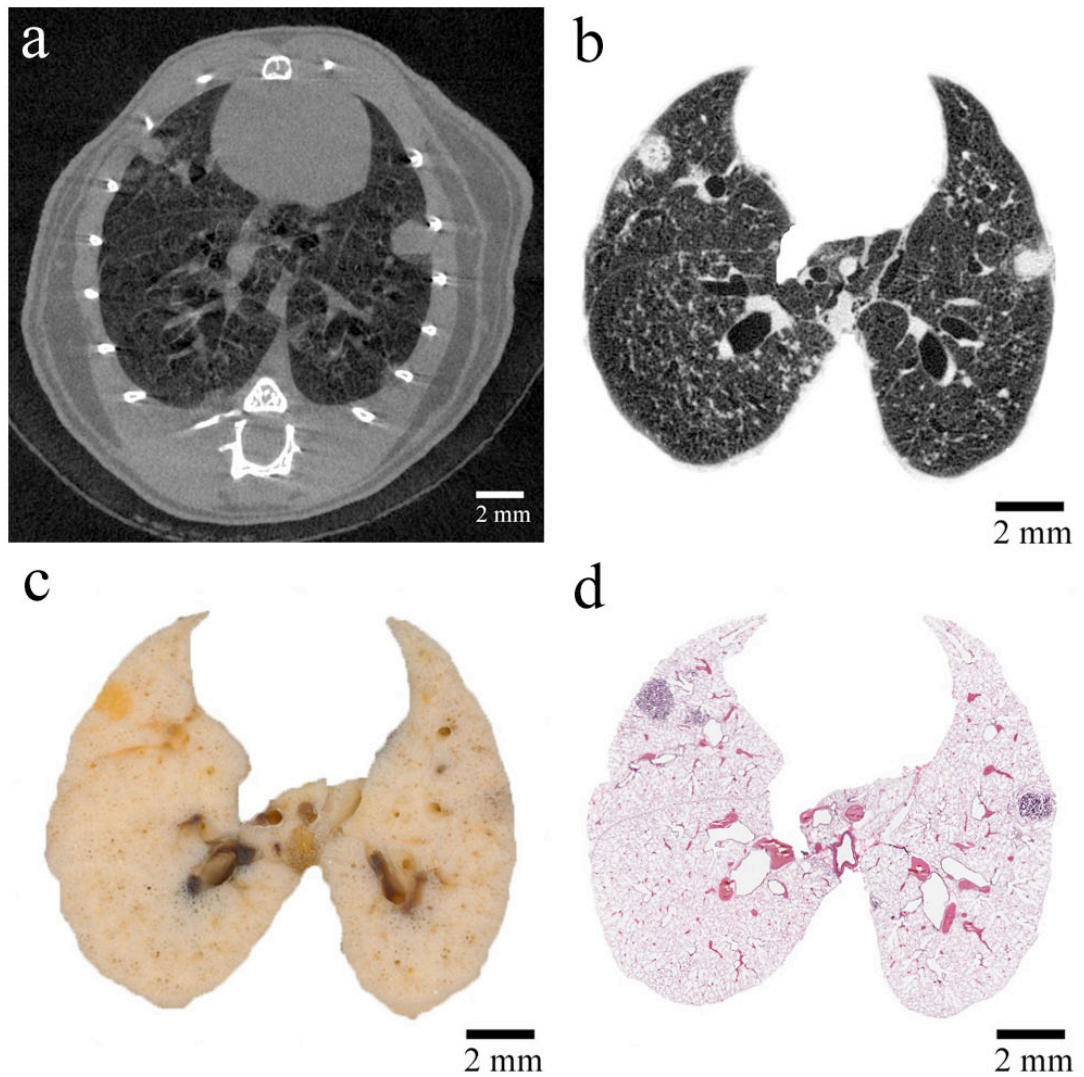


Figure 6.42: Registered (a) *in vivo* micro-CT, (b) fixed *ex vivo* micro-CT, (c) LIMA and (d) H&E Histology dataset from the six-month time point.

*In-vivo* micro-CT datasets from the same mouse shown in Figure 6.42 at time points 2, 3 and 4 months have also been registered, and an axial slice at each time-point is shown in Figure 6.43.

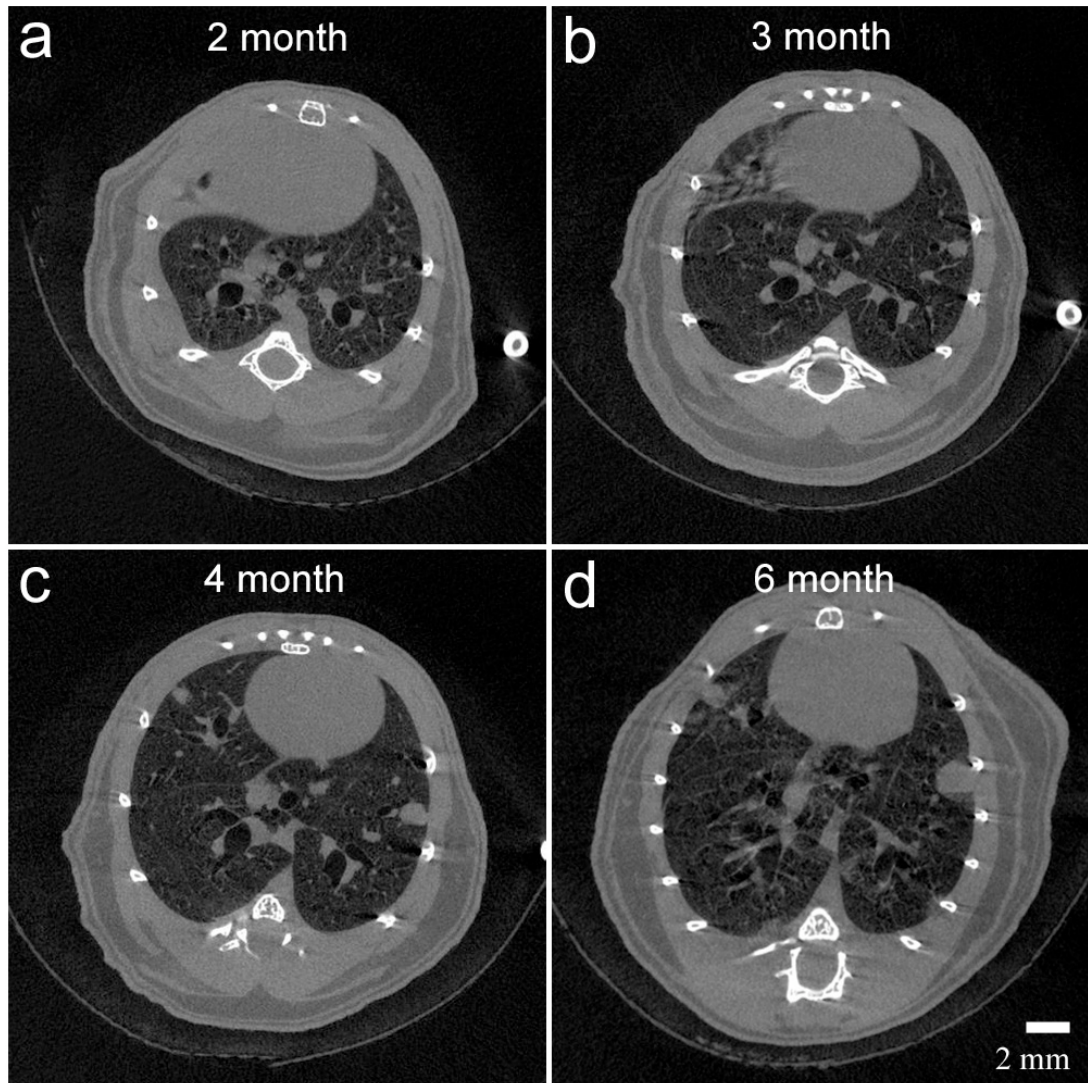


Figure 6.43: Micro-CT axial images at 2, 3 and 4 months post Urethane administration for the dataset shown in Figure 6.42.

### 6.3.5 Histology

LIMA sections from each lung were processed for H&E histology, and all lesions were examined with the assistance of an expert lung pathologist (Dr. Jamie Weydert).

Figure 6.44 represents an example for each of the different stages of tumor progression found in the Urethane mouse lung in this 6-month study and includes data from additional mice at 12-months to depict adenocarcinoma example.

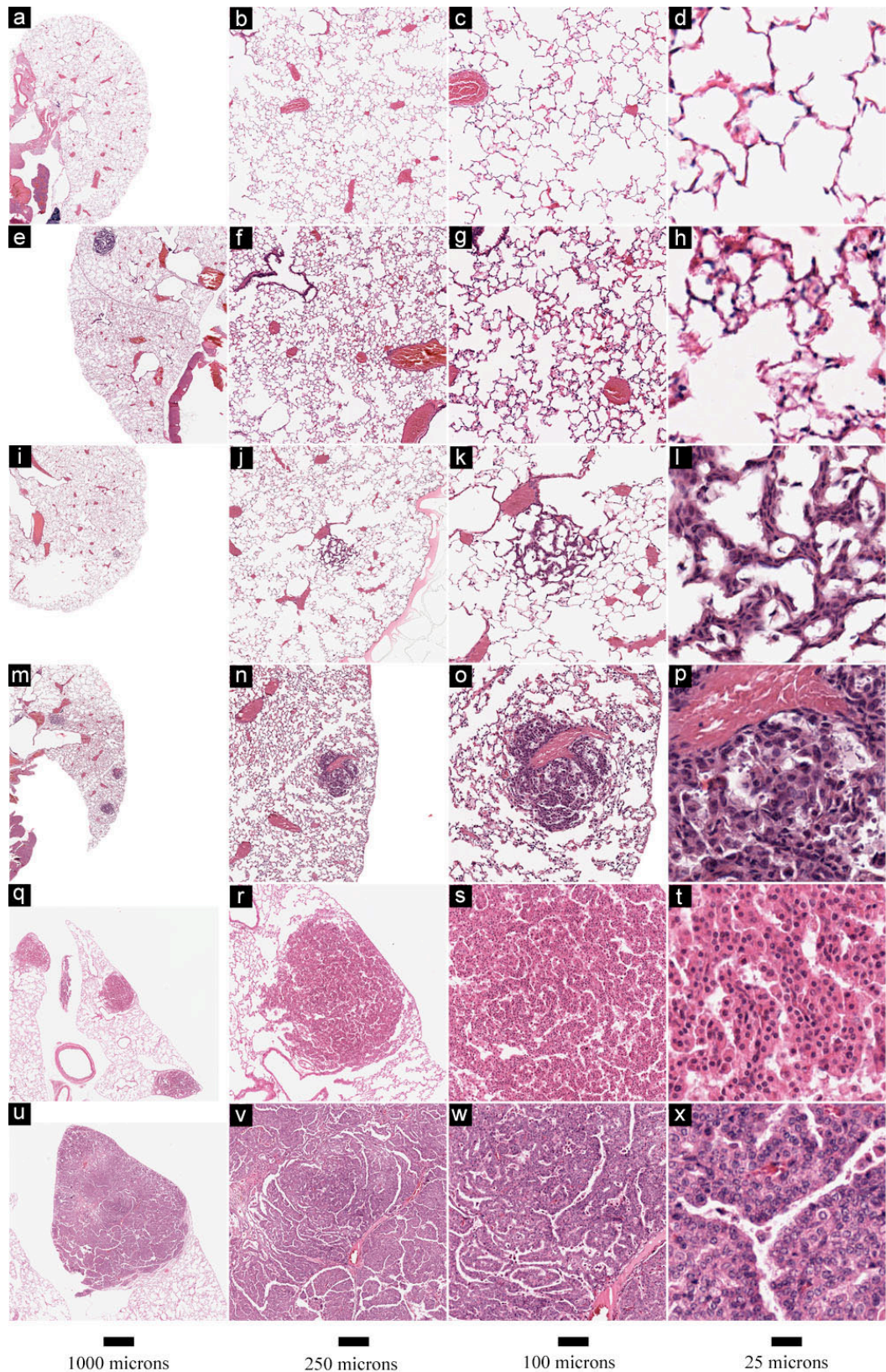


Figure 6.44: Urethane mouse lung histology at 6-months (a-d) normal parenchyma, (e-h) alveolar hyperplasia, (i-l) benign micro adenoma (<0.5mm), (m-p) benign papillary adenoma (>0.5mm), (q-t) pre-invasive adenoma (>1mm), (u-x) malignant adenocarcinoma at 12 months (>5mm).

The rate of growth for three unique tumors identified in the Urethane mouse lung dataset, illustrated in Figure 6.39, Figure 6.40 and Figure 6.41, are shown in Figure 6.45. The histology for each lesion in this example has been extracted from the registered datasets and illustrated in Figure 6.46 at 4x, 10x and 20x magnification.

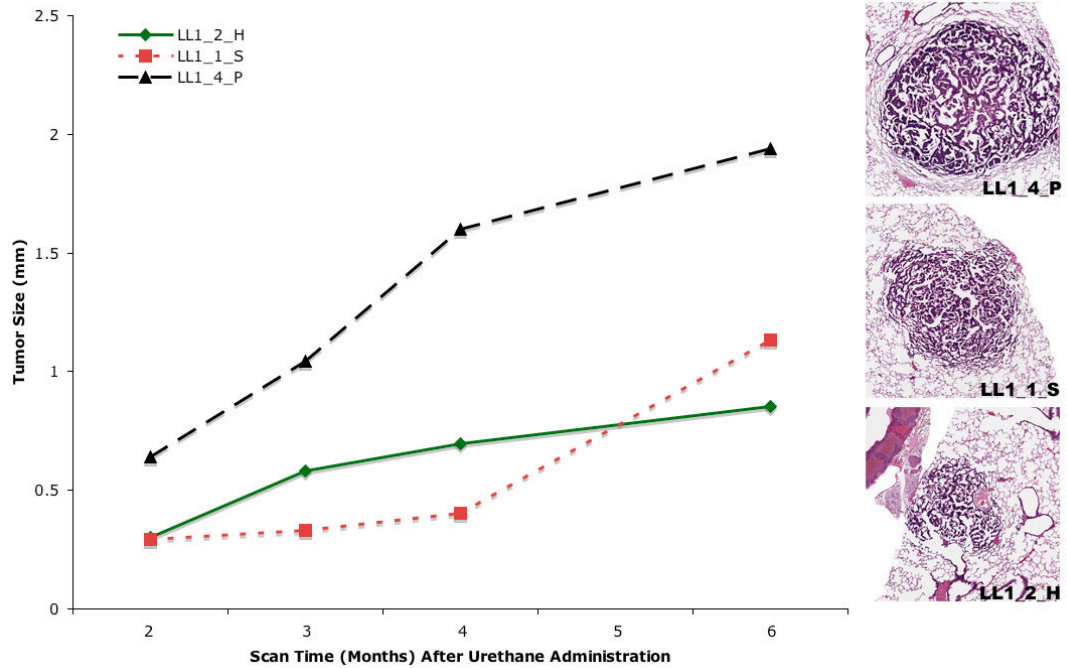


Figure 6.45: Tumor progression from three lesion identified in the left lung of the Urethane mouse lung shown in Figure 6.39, Figure 6.40 and Figure 6.41.

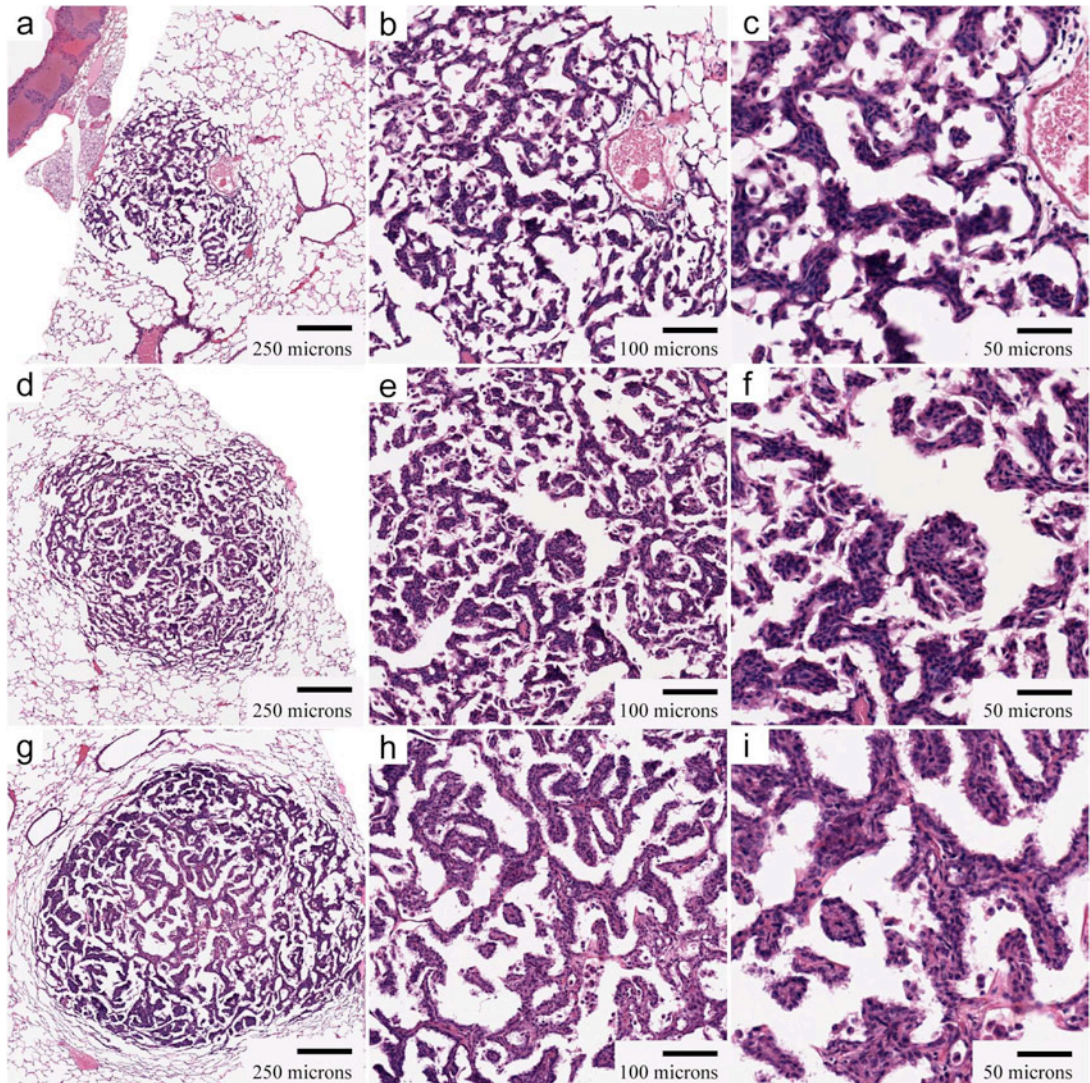


Figure 6.46: Magnified cascading (4x, 10x and 20x) histology from three six-month lesions as tracked and graphed in Figure 6.45. Panel (a-c) represents tumor LL1\_2\_H, (d-f) represents tumor LL1\_1\_S, and (g-i) represents tumor LL1\_4\_P.

The pathologist's interpretation of all the lung nodules from this study was that they were all adenomas with no adenocarcinomas identified in this 6-month study.

## 6.4 Discussion

### 6.4.1 Image Acquisition

Several critical improvements were made to the *in vivo* imaging techniques presented in Section 4.3 in order to facilitate an efficient, safe and low mortality longitudinal study. Two of the major changes were the anesthetic regime and intubation procedure.

#### **6.4.1.1 Anesthesia**

The use of ketamine / xylazine, isoflurane and pancuronium, provided a stable level of anesthesia for the non-survival *in vivo* study detailed in Section 4.3, but was problematic for this study as the recovery time was in excess of 2 hours per mouse, in preliminary experiments. Through investigation of previous studies in the literature and preliminary experiments, xylazine was replaced with medetomidine chloride. Also, isoflurane did not produce the prolonging compound anesthetic effect on medetomidine as was the case with xylazine. In addition, a high affinity reversal agent was available for medetomidine, providing a fast recovery option. The paralytic agent pancuronium bromide was also replaced with rocuronium bromide as this had a smaller half-life [215]. Rocuronium bromide provided sufficient paralysis for a single *in vivo* micro-CT scan, yet permitted fast recovery at the conclusion of the scan.

#### **6.4.1.2 Tracheal intubation**

Intubation of mice using techniques found in the literature, mainly laryngoscope guidance and light enhancement of the trachea, proved unreliable. The intubation technique was mastered only after many trials and finally through development of a micro-bronchoscope, which significantly increased the success rate of the intubation and reduced injury to the mouse during the procedure. Seemingly a small part of the overall study, this was a key technological development that allowed for the longitudinal study to be performed successfully with minimal mortality due to animal preparation. A drop of lidocaine (1% Lidocaine HCL, 10mg/ml) was also applied to the tip of the intubation catheter prior to intubation. This step provided local anesthesia to the vocal chords and reduced the chance of vocal chord spasm.

#### **6.4.1.3 Animal preparation**

In the initial micro-CT scans, it was found that some mice exhibited radio dense “nodules” or particles in the lung parenchyma. These “spots” were not considered physiologic lesions, but instead it was hypothesized that these particles had been

aspirated from the stomach during intubation. To reduce the likelihood of such an event occurring, mice were starved for several hours prior to micro-CT scanning. No radio dense particles were identified in future scans.

Prior to micro-CT scanning, the mice were also administered with 0.5cc of saline subcutaneously in the abdominal region. This step was added to prevent dehydration during scanning and promote faster recovery at the end of the scan.

### 6.4.2 Micro-CT Tumor Analysis

The micro-CT datasets acquired over time for the same mice were analyzed, and statistics on the tumor number, size, location and growth were extracted. The ability to track individual nodules over time, as shown in Figure 6.16, is useful for assessment of growth rates and precise correlation of growth rates with the underlying histology. The rich information content available in each *in vivo* micro-CT scan is illustrated in Figure 6.17 and Figure 6.18 from which identification of lesions can be made with respect to surrounding structures such as vessels, pleura and airways. From Figure 6.17, we can see the illustrated tumor has multiple large vessels surrounding its borders.

Based on the general statistical overview of this study shown in Table 3, it was found that detection and tracking of nodules as small as 0.112mm was accomplished, and the extraction of commonly calculated tumor size characteristics including, RECIST, Ortho, WHO, volume and average HU was successfully performed.

Examining the longitudinal RECIST, WHO and Volume data for individual nodules shown in Figure 6.19, Figure 6.20, and Figure 6.21, respectively, for one mouse, and in Appendix B for all mice in this study, a remarkable heterogeneity in tumor growth rates within mice is observed. For example, nodule LL1\_4\_P and RL3\_3\_S have a significantly greater growth rate when compared to all other identified nodules. Also, several of the nodules in this mouse are exhibiting a plateau in growth and some are reducing in size, for example LL1\_10\_P and LL1\_2\_H are hitting a plateau, while RL3\_4\_P and RL3\_7\_P are reducing in size. In addition, one

nodule (RL3\_9\_P\_D) has completely disappeared by the final time point as detected on the micro-CT dataset. In this study, similar to [216], we found disappearance of tumors to be a very rare event and only identified two such cases across the nine mice studied up to the 6-month time point and one in the fourth group of mice between months 6 and 9. Other studies investigating different mouse strains and carcinogens along with genetic models of lung cancer have regularly reported the disappearance of lung tumors. The primary difference between our findings and prior studies is the mouse model, however the results may also reflect the level of resolution in the images used for analysis. In the past, small microscopic adenomas were identified from histology to have regressed and may represent tumors smaller than the resolution of the micro-CT system i.e. below 100 $\mu$ m.

The number of tumors identified using the micro-CT imaging technique over the span of the 6-month study is shown in Figure 6.22. This data correlates well with previous studies by other groups on the A/J Urethane mouse model of lung cancer [216]. Here, we can see the rapid increase in nodules in the first three months with a slow increase in later months. Also illustrated in this graph and not shown in any previous study is the number of tumors identified at each time point within each lobe. Here, we can clearly see the significant difference in tumors within the left lung and right diaphragmatic lobe as compared to the right apical, azygous and cardiac lobes.

To investigate whether the incidence of tumors within a lobe was directly related to the size of the lobe, and hence determine whether the presence was likely to be randomly distributed, a comparison of the lobe volumes versus tumor incidence for each lobe was carried out. The lung volume (including air and tissue) for each lobe of a normal adult A/J mouse was determined through manual segmentation of the lung wall and fissures from an *in vivo* micro-CT scan. The percentage of each lobe was calculated with respect to the total lung volume. Figure 6.23 represents the tumor incidence across all mice scanned in this study versus the lobe volume percentage for the normal adult A/J mouse. With the limited lobe volume data, statistical significance cannot be determined, however from these initial results it appears there is a very strong correlation between tumor incidences within lobes versus the lobe volume.

An interesting observation was that the diaphragmatic lobe has a twenty percent greater rate of tumor incidence with respect to lobe volume as shown in Figure 6.23. Furthermore, during the span of this study, the right diaphragmatic lobe grew significantly in the mouse lung cancer model, illustrated in an example in Figure 6.32. The growth of this lobe was greater than the total tumor load and may be a response to compensate for the reduced lung function.

The aggregate average growth rate for all tumors identified in this study followed a linear rate for the first 2 months and began to slowly decrease in growth rate up to the 6 month time point as shown in Figure 6.24. We also observe from Figure 6.24 that the distribution of tumor size increases with time as depicted by the spreading whiskers and outliers. This was expected as some tumors grew at a slow rate, some stopped growing altogether and even regressed, while others had an aggressive progression. The overall median trend, as represented by the central bar in the box plot, reveals a slow down in growth at the 4 and 6-month time point. This is a direct consequence of the superposition of the greater number of slow growing tumors versus the few aggressive tumors identified within each mouse.

From Figure 6.25, the heterogeneity in the tumor size within the left lung and the right diaphragmatic lobe is apparent since the standard deviation and the number of outliers is greater as compared to the other right lobes. This is consistent with the increased number of tumors identified in both these lobes, which could be leading to a greater probability of tumor heterogeneity. Further investigation between the structural and biological differences between these two larger lobes versus the three smaller right lobes should be undertaken.

The general growth rate appears to be similar across the lobes, as shown in Figure 6.26, representing the mean tumor size versus time for each lobe. Closer examination of the azygous lobe reveals that growth may be reaching a plateau, whereas growth in other lobes is still increasing at the 6-month time point. This may be due to any number of factors not limited to the lobe size, location, vascular system and supply, all of which require further investigation. The number of outliers

is also significantly greater in the left lung and right diaphragmatic lobes, indicating greater heterogeneity of tumor size within these lobes.

From the histogram of tumor size in Figure 6.27, there is an indication of three groups of nodules with respect to size across all lobes. The third group representing the larger tumors is expected to become more prominent with the addition of data at further time-points.

Figure 6.28 reveals the distribution of tumor size versus each lobe. Here, the difference in growth of tumors within lobes becomes apparent. The distinct tumor size groups in the histograms that emerge within each lobe follow a similar pattern. With the exception of the azygous lobe, all other lobes contain at least two local maximums indicating multiple growth rates.

In Figure 6.29, we observe the change in tumor size distribution over time. Here, not only can we clearly see the shifting to the right from small nodules to the occurrence of larger nodules, but also the development of two groups at the 6-month period, represented by the two peaks. We can postulate that aggressive tumors in the second group will continue to grow and this distinction will become increasingly greater over time. At further time points, a third group of tumors may emerge, representing large slow growing tumors that remain benign and do not further transform to adenocarcinomas.

Based on the test of Fixed Effects on the RECIST data, there is no lobe-time interaction and tumor growth is observed to be parallel, while the Volume data suggests non-parallel growth. Here, we can clearly see a significantly different outcome based on two tumor size metrics. Considering all metrics are calculated on the same set of tumor boundaries, it is evident that new measures of tumor size or evaluation techniques are needed. In this study, the tumor volume provided a better distinction between slow and aggressively growing lesions, providing further evidence for the utility of measuring tumor volume, a 3D descriptor rather than traditional 2D descriptors.

There were no tumors identified from the four normal A/J mice used as the control in this study by the 6-month time point, and therefore no analysis has been shown from these mice.

### **6.4.3 Micro-PET & MRI**

#### **6.4.3.1 PET Imaging**

PET imaging was performed on three mice in this study at the 6-month period to provide pilot data for future studies. Initially, it was hypothesized that even though the majority of tumors would still be in the adenoma phase at 26 weeks post Urethane administration, some FDG uptake would still be detectable at this transitioning period. Surprisingly, it was found there was no measurable uptake in the lung at this time point.

Uptake of  $^{18}\text{F}$ -FDG into the heart was a primary concern and obstacle for this modality, particularly when the 6-month PET scans were negative in the lung region. Initially, it was thought that the heart uptake was “drowning” the detection within the lung. This may still be the case, but the follow up 9-month scan (Figure 6.31 (c)) reveals strong uptake in both lungs with nodules that are comparable in size with respect to the 6-month time point as seen in the micro-CT images in Figure 6.32. FDG uptake associated with tumor progression in these examples is not conclusive and may be due to global inflammation in the lung in response to the Urethane and or tumor load.

The dramatic increase in the lung volume between the 6 and 9-month scan is also striking, as seen in Figure 6.32 (c). The combined tumor volume was calculated to be  $10.8\mu\text{l}$  at 6 months and  $20.1\mu\text{l}$  at 9 months, while the lung volume had increased from  $805\mu\text{l}$  at 6 months to  $1301\mu\text{l}$  at 9 months. The over 60% increase in lung volume at the same inflation pressure was an interesting observation. One possible explanation for the increase in lung volume could be hyperinflation of the lung as a result of the many obstructed airways due to small tumors. Further investigation into this observation is needed.

From previous literature, it is known that tumors from the Urethane mouse model transition from the adenoma to adenocarcinomas phase between 25-45 weeks. From the negative PET activity observed at the 6-month time point and the positive PET activity at the 9-month time point seen in Figure 6.31 (c), we hypothesize that PET activity is likely negative until this critical transition, or lesions are too small to be detected with the current PET imaging system.

### 6.4.3.2 MRI Imaging

Three mice underwent MRI imaging at the six-month time point in order to determine the sensitivity of small animal MRI in detecting and potentially differentiating lung tumors.

From Figure 6.33 (a) & (b), we can clearly appreciate the advantage of using micro-CT as opposed to micro-MRI for identification and tracking of sub-millimeter tumors. As shown in the examples, there are multiple nodules in the order of 0.5-1.5mm identified in the micro-CT scan, which can barely be seen in the micro-MRI scan. We should note that the micro-CT scan was performed using the IIBH respiratory gating technique, while the micro-MRI scan had no gating applied. Implementing respiratory gating for the micro-MRI scanning would significantly increase the resolution and ability of identifying and tracking nodules. From previous studies, we know that even with respiratory-gated micro-MRI imaging, lung nodules smaller than 0.4mm can not be resolved [202]. In the current study, we were only able to resolve nodules as small as 0.8mm in the micro-MRI images without respiratory gating.

Micro-MRI imaging does provide several advantages over the micro-CT imaging technique. MRI is a non-ionizing imaging technique, removing the potentially adverse effects of X-ray imaging on the mouse and underlying cancer biology. Also micro-MRI can provide greater soft tissue contrast, but this was not apparent in our study predominantly due to the lack of gating. Finally, scan times are shorter when compared to standard *in vivo* micro-CT scanners, but with respiratory gating the acquisition times would become more comparable.

In the current study, the MRI images did not provide greater identification of tumors or the ability to differentiate tumor sub-type. MRI used as a complementary modality for late stage tumor development in nodules greater than 1mm, could prove highly useful. In particular, the high soft tissue contrast would be important for assessing tumor sub-types, and potentially the use of functional imaging techniques, such as hyperpolarized gas, may provide additional information about the underlying biochemical processes in and around the tumors.

#### 6.4.4 LSCM Imaging

Mouse lungs were imaged *in vivo* using the CBCM technique outlined in Section 5.3 and further described in Section 6.2.6.4. At the completion of CBCM imaging, the lungs were excised and re-imaged using the LSCM technique outlined in Section 5.2. This was the first time laser scanning confocal microscopy had been performed on this mouse model of lung cancer *in vivo* or *ex vivo*; this provides a foundation for future studies that may translate into clinical optical biopsy procedures.

The initial CBCM imaging protocol included FITC, PKH26-PCL and Draq5 staining, but early in the study it was concluded that the Draq5 nuclear stain had a very broad excitation spectra, which resulted in quenching of light from the FITC and PKH26-PCL emission. The protocol was then altered to use FITC, Acridine Orange and PKH26-PCL. After further evaluation, it was found that a combination of the low quantum efficiency of the PKH26-PCL dye, the limited power 543nm diode laser used for excitation, and the loss of power for excitation and emission through the fiber bundle, caused the PKH26-PCL emission signal detected to be very low using the CBCM technique. Imaging through the LSCM chamber was successful and produced images with much greater signal to noise for all of the stains discussed above, as seen in Figure 6.35, Figure 6.37 and Figure 6.38. In contrast to CBCM imaging, the macrophage staining was not reliably detected and further investigation and development is required for visualization of macrophage activity using the fiber based approach.

For the CBCM imaging of the lung cancer nodules, it was later found that by using only the FITC systemically and Acridine Orange nuclear stain topically a bright and

informative image could be attained. In particular, the shift in emission spectra of the Acridine Orange stain when bound to ssDNA as opposed to dsDNA provided an informative picture of the cell cycle activity.

Differentiation between normal, suspicious and tumor tissue using the CBCM technique was quite evident using this imaging protocol. Two prominent differences were visually identified. The first was the noticeable increase in nuclear number when moving from normal, to suspicious, to tumor regions. The second was the increase in the number of red shifted nuclei (blue/purple in the images), representing an increase in single stranded DNA bound Acridine Orange. The increase in ssDNA indicates an increase in mitoses, an observation inline with the phenotype of cancer cells.

Figure 6.34 represents two mice lungs, the first image (a) represents alveolar parenchyma from a normal A/J mouse, while (b) represents normal alveolar parenchyma from a tumor bearing Urethane mouse lung. Here, it is clear that the number concentration of ssDNA (blue) is greater in the Urethane lung as opposed to the normal A/J mouse lung. This suggests a “field effect” from either the administration of the Urethane or the presence of lung tumors in the Urethane mouse. A recent study also found a “field effect” in the Urethane mouse lung cancer model. In their study, they identified an increase in neutrophils in the “normal” parenchyma with an increase in the number of neutrophils and macrophages surrounding the tumor [217].

The suspicious region shown in Figure 6.34 (c) and the tumor region in Figure 6.34 (d) have distinct differences with respect to the “normal” region in Figure 6.34 (a). One of the predominant characteristics between these images includes the unordered and solid tissue structure that does not follow the alveolar pattern observed in normal regions. There also exists a greater number of nuclei, particularly nuclei emitting in the red fluorescence (indicated in blue on the images). Further investigation into the underlying histology at these locations needs to be undertaken, for accurate correlation of images acquired using the presented CBCM technique with known cellular structures.

In Figure 6.35, the LSCM imaging chamber is utilized in a similar example where lung parenchyma from a normal A/J mouse is compared with normal parenchyma and tumor tissue from a Urethane mouse lung. Here, the lack of cells and nuclei with ssDNA in the normal mouse, as opposed to the prevalence of ssDNA in the Urethane mouse lung, is clearly evident. The size and heterogeneity of the nuclei in the normal mouse versus Urethane mouse is also apparent. This heterogeneity is more prominent in the tumor regions where the nuclei are clearly larger and appear in a range of colors and sizes, indicating a mixture of dsDNA and ssDNA within the same cell.

A low magnification LSCM example of a tumor from a Urethane mouse lung at 6-months is shown in Figure 6.36. Here, clear depiction of the tumor boundary and surrounding alveolar structure is visible. The heterogeneity in the tumor morphology and emission of the Acridine Orange nuclear stain is also clearly seen in this example. An interesting observation is the emission of the Acridine Orange and the prevalence of the blue/purple (ssDNA) nuclei on the tumor surface and its surroundings. Simultaneously, there is a small region between the tumor boundary and the surrounding alveolar parenchyma that exhibits an increase in green/orange (dsDNA) nuclei. The increasing septal wall thickness as we move closer to the tumor is also observed and is consistent with the thickening of septal walls identified in the high magnification examples in Figure 6.35. The protruding structures on the pleura (left side of the image) are unknown at this stage, and may represent pleural connective tissue that is now floating in the PBS bath.

A high magnification example using the LSCM imaging technique is presented in Figure 6.37. Here, a normal region (a) and tumor region (b) from a Urethane mouse lung are shown. Four stains were used in this example: FITC was injected systemically for general tissue contrast, PKH26-PCL was injected 24 hours prior to imaging intra venously, and Draq5 and Acridine Orange were topically applied over the region of interest. Alveolar macrophages were not detected in this example, a result of their absence or weak signal from the PKH26-PCL dye. The combination of the Acridine Orange and Draq5 staining did produce a dramatic image where a combination of both is present in many of the cells, indicating a range of dsDNA and ssDNA within and across the cells. Again, further investigation of the

underlying histology needs to be undertaken in a future study to identify the cellular structures seen using this technique.

A LSCM example with prominent detection of alveolar macrophages is shown in Figure 6.38. Here, only FITC and PKH-26 were administered, and the tissue was imaged using the LSCM technique. The figure represents a region between a tumor in the azygous lobe and the adjacent normal parenchyma in the diaphragmatic lobe. It is clear from this example that the number of alveolar macrophages is multiple orders greater just beneath the tumor surface as opposed to the “normal” alveolar airspace. Further investigation of macrophage activity would be highly informative. In future studies, the use of high-speed LSCM systems may enable tracking of alveolar macrophages in and around the tumor, providing dynamic observation of underlying cellular activity, an important avenue of research.

An unexpected finding when comparing parenchyma from a normal A/J mouse to the Urethane mouse lung was the increase in alveolar airspace size. With the limited sampling across the lobes and lungs in the normal regions, further investigation is needed to make this finding conclusive. This observation was consistent in this study and reflected in the examples presented in Figure 6.35 and Figure 6.37. Along with the increase in alveolar airspace, there was also an increase in alveolar wall thickness as seen in Figure 6.35 (b). Both these structural changes could be used in future studies to assess the “field effect” of tumor bearing lungs over time in “normal” regions.

Initially, when imaging tumor regions using the CBCM system, nuclei were not always visible, as shown in Figure 6.47 (a). It was later found that slight pressure was required between the fiber optic probe and the tumor for positive nuclear imaging as shown in Figure 6.47 (b).

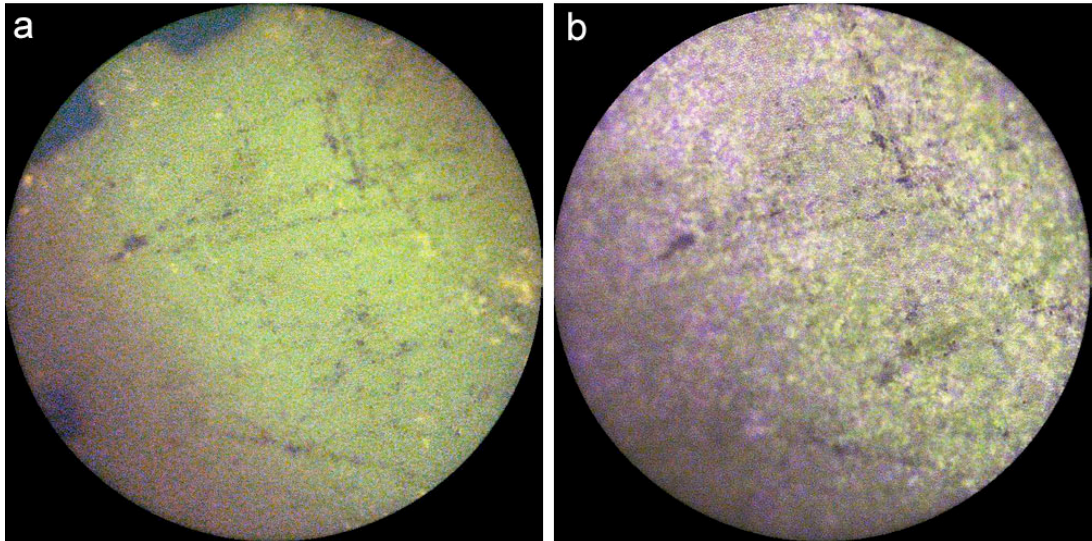


Figure 6.47: CBCM image over a tumor region with (a) no pressure applied to the probe and (b) with slight pressure applied to the probe.

It was hypothesized that a layer of tissue or liquid was preventing the probe from exciting / detecting the nuclei. This was a limitation of using a surface fiber optic probe, as opposed to a dynamic micro-objective probe to provide control over the depth of imaging. In such a situation, the axial resolution would be reduced and the ability to control imaging beneath the surface would be available. Future studies using a sub-surface probe should be undertaken to circumvent this limitation and provide greater information on the cellular structures in solid tissue beneath the surface.

These qualitative results indicate that significant obvious changes are present and detectable by confocal microscopy in this mouse model of lung cancer. This suggests that translation to the human lung and human lung cancer is likely to be both possible and informative.

#### **6.4.5 LIMA Imaging**

Using the methodologies described in Chapter 3 and further detailed in Section 6.2.6, each lung in this study was fixed, embedded, micro-CT scanned, LIMA imaged, sectioned and processed for H&E histology.

Using the foam embedding technique detailed in Section 6.2.6.5, as opposed to the agar embedding described in Section 3.2.8, provided additional support between the *ex vivo* micro-CT imaging, the subsequent LIMA and histology sectioning and imaging. This resulted in strongly aligned data across these imaging modalities with no computational registration required. However, the addition of the foam did introduce artifacts in each imaging step. During the micro-CT imaging, the foam slightly reduced the overall clarity of the micro-CT images due to the diffractive manner at which the X-rays interacted with the foam. In the LIMA, imaging the foam was very similar in color to the surrounding lung tissue. Finally, in the histology the foam stuck to the lung parenchyma and remained on the slide during slide digitization. With the additional pre and post processing steps outline in Section 4.2 for the micro-CT, the added noise was not significant. The addition of Indian ink into the polyurethane foam process increased the contrast between the foam and the lung during the LIMA imaging. Finally, the foam was digitally extracted post histology slide acquisition. Overall the benefits of maintaining orientation between these modalities were far greater than the few problems discussed above.

With the registration process outlined in Section 6.2.9, the *ex vivo* datasets were accurately registered back to the original *in vivo* datasets, providing a comprehensive dataset representing the same position in the lung from *in vivo* down to the histology as shown in Figure 6.42. Considering the complexity of registering this wide variety of imaging modalities, an efficient process was developed where each complete dataset was organized, registered and transformed in one sitting.

An unexpected pattern that was observed in many of the Urethane mice in this study was the initial onset of atelectasis or inflammation in the upper regions of the lung. These same atelectic regions tended to exhibit large nodules in future scans. Although, with the high number of nodules per mouse, this was not conclusive and further investigation is required. An example of this phenomenon can be seen in Figure 6.43.

### 6.4.6 Histology

After analysis of H&E histology from mice lungs bearing tumors, it was found that there existed a mix of pulmonary lesions using the Mouse Models of Human Cancers Consortium (MMHCC) classification scheme [96]. These included: alveolar hyperplasia, papillary benign adenomas, and finally from mice lungs at 9 and 12 months with pre-invasive adenomas and adenocarcinomas. An example of each is shown in Figure 6.44. Figure 6.44 (a-d) represents a region of normal lung parenchyma from a Urethane mouse lung. The region exhibiting hyperplasia (e-h) shows an increase in cells lining the normal alveolar septal architecture. The micro adenoma (i-l) represents a region with a focal hyperplasia under 500 microns, while the benign adenoma (m-p) represents a lepidic focus greater than 500 microns with some papillary structure and compression of the surrounding parenchyma. The benign papillary adenoma (q-t) represents a region greater than 1mm with a papillary pattern, a well-defined border, compression of the surrounding parenchyma and pre-invasive potential. The adenocarcinoma from a 12-month mouse (u-x) is characterized by a large lesion of 5mm and greater with prominent cytological atypia, increased frequency of mitoses and greater papillary structure. No direct evidence of invasion or desmoplasia was identified in this example, and given the lack of malignant features in the classification paper [96], this could also be classified as a pre-invasive adenoma; however, based on papers published by other groups using the Urethane mouse lung cancer model [100, 202, 216, 217], this lesion would commonly be classified as an adenocarcinoma. Clearly there exists a wide discrepancy between classification of tumor histology in mouse models of lung cancer, and further refinement is needed.

For the first 6 months, it was concluded that the predominant type of lesion found in the Urethane mouse lung cancer model was benign papillary adenomas of varying sizes with no malignant tumors identified, a finding inline with previous studies [100]. In this case, there was proliferation of the alveolar septa with large uniform cells incorporating round to oval nuclei, and the structure of the underlying alveoli could still be identified in these examples. In very few cases with large nodules, there was some premise for pre-invasive structure where large uniform populations of epithelial cells were found in concentrated regions throughout the tumor, but this was not definitive.

One objective of undertaking this study was to relate growth rates of individual tumors back to their respective histology as this would provide valuable insight into understanding factors influencing the initiation and progression of lung cancer. Also, identifying adenocarcinomas that arise from early adenomas versus those developed from unique sites would provide valuable insight into the underlying cancer biology. Tracking each lesion over time using the *in vivo* micro-CT imaging and correlating to the respective histology through the LIMA registration protocol has been successful. An example of three lesions tracked over time within the same lung is shown in Figure 6.45 and Figure 6.46. Here, the growth rates are represented in the graph in Figure 6.45 and the respective histology for each lesion at the 6-month time point has been illustrated at varying levels of magnification in Figure 6.46. Although growth rate and tumor size are strongly related to the tumor progression, an observation found in previous studies [202], the majority of lesions in this 6-month study were classified as benign papillary adenomas. This homogenous classification prevented obvious differences to be identified based on the H&E histology tumor phenotype. Further investigation using immunohistochemistry staining and genetic expression profiling of adjacent slides should be undertaken in future studies and correlated with growth rates, to determine if a distinction between fast and slow growing tumors can be made. Addition of data from longer time-points would also be highly useful and link tumor growth rates with the transformation from an adenoma to an adenocarcinoma. Finally, investigation of surrounding structures such as airways, vessels and pleura needs to be undertaken and related to the growth rates of individual tumors.

Using the data acquired in this study, comparison of tumor metrics such as the RECIST and Volume measurements can also be made and correlated with histologic outcomes. Currently, assessment of tumor progression based on size change has come under scrutiny and requires further objective analysis. In addition, correlation of tumor diameter and volumes using the *in vivo* and *ex vivo* micro-CT data versus the histology would provide further data on the accuracy of the *in vivo* micro-CT imaging system for measuring tumor metrics. Finally, an un-blinded re-read of the micro-CT data using the registered histology images as a reference would be

valuable for determining the limitations of the micro-CT imaging system in detecting lung tumors *in vivo* and *ex vivo*.

## **6.5 Conclusions**

An array of imaging techniques, protocols and devices have been described and developed in order to successfully conduct longitudinal pulmonary imaging in mice for the assessment of structure, function and pathology.

A comprehensive mouse lung cancer study has been undertaken utilizing the *in vivo* micro-CT imaging techniques developed in Section 4.3. 250 unique tumors have been identified and tracked for growth in the same mice over a period of 6 months. Tumors as small as 0.112mm have been accurately identified, providing an incredibly powerful technique for the detection and tracking of early lung cancer in mice.

The intra-mouse tumor growth rate exhibited a high heterogeneity with a mix of slow growing, regressive, disappearing and aggressive tumors identified over a 6-month period. Tumors were accurately registered to their respective underlying histology using the image acquisition and registration processes, described in Chapter 3, integrating the LIMA system. This enabled correlation of individual tumor growth rates with the H&E tumor phenotype, a task not possible when utilizing standard sacrificial pathology techniques. In this study, it was determined that no difference between tumor phenotype based on H&E histology and published classification schemes with respect to growth rates could be found within this 6 month study. In previous studies, tumors in this mouse model are observed to remain in the adenoma stage at 6-months post Urethane administration, and do not progress into adenocarcinomas until 8-months+. However, we hypothesize the existence of underlying genetic, molecular and cellular differences before this transformation. We plan to further investigate this hypothesis on the data acquired in this study through the utilization of immunohistochemistry and genetic expression evaluation on adjacent histology slides to reveal potential differences in tumor and inflammatory cell populations with respect to growth rates.

Utilizing several tumor size metrics enabled both re-evaluation of growth rates using different size estimates, but also provided an indication of the variability in assessment outcomes due to tumor size metrics, a major concern in the clinical situation.

Pilot data was acquired utilizing micro-MRI and micro-PET imaging on a subset of the mice in this study, providing valuable results for planning future studies.

Finally, the first *in vivo* and *ex vivo* imaging of tumors in the Urethane mouse lung cancer model using laser scanning confocal microscopy was completed. A significant difference between normal parenchyma from control mice versus Urethane tumor bearing mice was identified. Differences between 'normal', suspicious and tumor regions were even more dramatic with greater nuclear number, tissue growth and change in nuclear staining spectral emission observed. From these initial studies, we are enthusiastic about translating this approach into the clinical setting for minimally invasive optical biopsy of lung cancer. Further systematic work is needed, including the development of catheter based multi-photon endo-microscopy system as well as fluorescent biomarkers that are safe for human use.

